Characterizing Spin Wave Propagation in Lithium Aluminum Ferrite Thin Films

CNF Summer Student: Anabelle Brueggemann
Student Affiliation: Department of Physics, Lafayette College

Summer Program(s): 2026 Cornell NanoScale Facility Research Experience for Undergraduates (CNF REU) Program

Principal Investigator(s): Gregory Fuchs, Cornell University

Mentor(s): Yinshi Chen

Primary Source(s) of Research Funding: CEEMag EFRC

Contact: gdf9@cornell.edu, alb477@cornell.edu, yc2793@cornell.edu

Summer Program Website(s): https://www.cnf.cornell.edu/education/reu

Research Group Website: https://fuchs.research.engineering.cornell.edu/

Primary CNF Tools Used: MLA150 Maskless Aligner, Oxford 81 Reactive Ion Etcher, AJA1 Sputter Tool, Sonicator, DSCO dicing saw

Abstract:

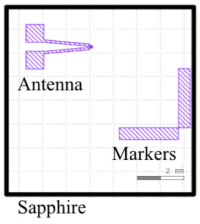

Lithium Aluminum Ferrite (LAFO) is a material that has emerged as interesting for applications in magnonics. Its low magnetic damping rate makes it ideal for magnon transport. The goal of this project is to investigate the nature of magnons propagating through LAFO. Scanning nitrogen-vacancy (NV) microscopy will be paired with coplanar waveguide readouts to image and quantify these spin waves. The first task is to fabricate a microchip stack that includes the LAFO thin film sample, coplanar waveguides to excite/readout spin waves, and a global microwave antenna to enable magnon detection. The LAFO is patterned using photolithography and ion milling, while the coplanar waveguides and the global antenna are fabricated using photolithography, metal deposition, and lift-off. The motivation for these experiments is the development of next generation, magnon-based interconnects for low-energy, intermediate scale data transfer.

Summary of Research:

As electronics scale down, copper interconnects have increasingly higher resistance, decreasing the efficiency of data transfer between devices. One mission of the "Center for Energy Efficient Magnonics" (CEEMag) is to investigate energy efficient interconnects in microelectronics that use spin waves, or magnons. Lithium Aluminum Ferrite, or Li0.5Al1.0Fe1.5O4 (LAFO), is the primary material we are investigating. It is a spinel ferrimagnet, and has an extraordinarily small Gilbert damping constant of about 0.004 (O'Mahoney et al.). This allows magnon propagation on an intermediate scale. We aim to characterize spin wave propagation in LAFO to explore its possible application in interconnects.

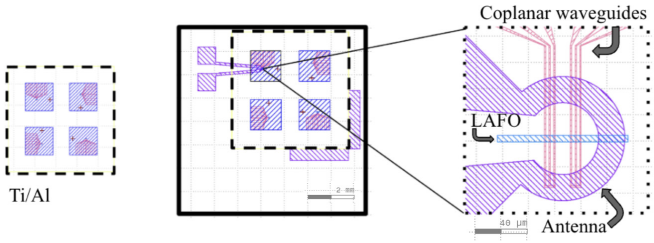

Figure 1: Chip Stack Design.

Our chip stack was fabricated in the Cornell Nanoscale Facility. The bottom layer of the chip, outlined in a solid line in Figure 1, hosts markers to place the top layer and a global antenna that will carry an RF signal. The top layer, outlined in a dashed line in Figure 1, has four identical sample sections, each with two coplanar waveguides, and a 100 by 1 micron sample of LAFO. The LAFO film, with a thickness of 35nm, sits above the antenna, with a 500 micron offset. An RF current is sent through the first waveguide, exciting a magnon that propagates 20 micrometers along the LAFO sample to the second waveguide which gives a time-domain of the magnon's amplitude. The underlying antenna emits an RF signal that interferes with the stray field produced by the magnon to aid in the scanning NV readout.

Scanning NV microscopy uses a point defect in diamond to detect micromagnetic properties of materials. This defect, the nitrogen-vacancy center, consists of a nitrogen substitutional atom with an adjacent carbon vacancy. Electrons in this center are sensitive to the surrounding magnetic field through their spin. In the scanning NV microscopy setup there is a diamond probe with an NV center at its tip, shown in Figure 2. The magnon produces an oscillating magnetic field with a constant

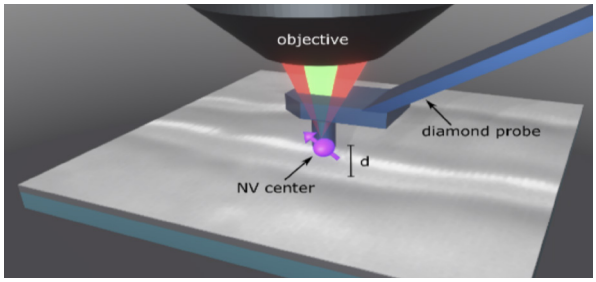

Figure 2: Scanning NV Probe.

spatial amplitude, but spatially varying phase. The NV center cannot detect this phase directly. Therefore, we need the global antenna to emit an RF signal which interferes with the stray field. This interference results in a static signal with a space-dependent amplitude. This signal is detected with the NV center to give a spatial image of the sample's micromagnetism. Pairing this with the electrical readout from the coplanar waveguide we can investigate how the magnon is propagating through the LAFO.

The fabrication of the bottom layer chip is done on a sapphire wafer. Layers of LOR3a and S1813 photoresist are deposited. The pattern is then exposed using the MLA150 maskless aligner and developed in AZ 726 MIF. Residual resist is removed with an oxygen plasma in the Oxford 81 reactive ion etcher. Next, the AJA1 is used to sputter on 10nm of titanium and 150nm of platinum. Finally, the lift-off of excess metal is facilitated by heating in 1165, and sonicating in 1165 and IPA. The devices are diced with the DSCO saw to fit into the printed circuit board, which can be placed in the scanning NV setup for measurements. The finished devices can be seen in Figure 3.

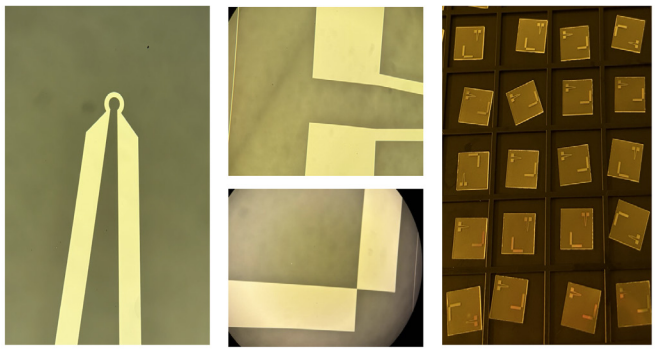

Figure 3: Fabrication Results.

In addition to this work, we have begun Mumax+ micromagnetic simulations to understand the physical meaning of future measurements. This aspect of the project is still developing, but the simulations show interesting effects.

Images in Figure 4 show samples of a different size than in our experiment to emphasize the pattern in the center of the sample, rather than the boundary effects. The bottom image in Figure 4 represents a continuous driving signal from the waveguide. Boundary magnetic conditions, edge reflections, and coplanar waveguide geometry could be causing the variations seen along the edges of the sample. The upper images in this figure use a one nanosecond driving pulse. The top left image represents a pulse from the current coplanar waveguide geometry. The top right image represents a pulse from a waveguide without ground lines. The interference that appears around four nanoseconds in the left plot, but not in the right, suggests that these ground lines may be problematic. While there are more simulations to be done, these results may motivate the fabrication of new devices with altered coplanar waveguides.

Conclusions and Future Steps:

The current focus of this project is determining the parameters for scanning NV measurements. The RF signals and bias field needed for the experiment must be found before data is collected. Additionally, there is continuing work on mumax+ micromagnetic simulations.

After characterization of magnons in LAFO, the next step will be to test transmissions of spin waves at the boundary between LAFO and another material. This will build further understanding of how magnons behave at the interface between the propagation material and the material used for magnon detection.

Acknowledgements:

This work is supported by CEEMag at SLAC National Accelerator Laboratory, Cornell NanoScale Facility, Cornell University, and grant DE-AC02-76SF00515.

References:

[1] O'Mahoney, Daisy, et al. "Aluminum Substitution in Low Damping Epitaxial Lithium Ferrite Films." Applied Physics Letters, vol. 123, no. 17, 2023, article 172405. https://doi.org/10.1063/5.0163362.

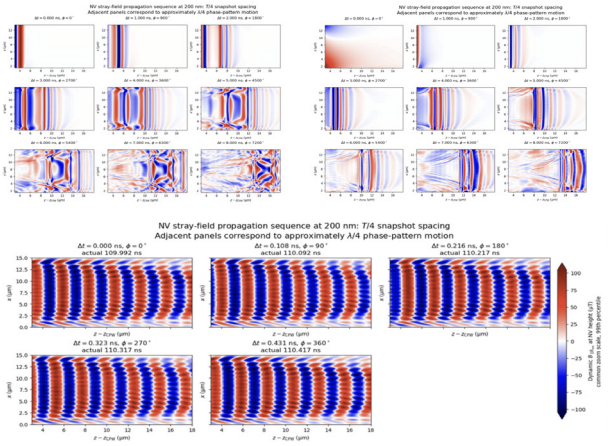

Figure 4: Preliminary Simulation Results.

Silicon Interposer for Millimeter-Wave Heterogeneous Integration: Doped vs High Resistivity Substrates

CNF Summer Student: Aditya Chembravattom
Student Affiliation: Department of Chemical Engineering, University of Florida

Summer Program(s): 2026 Cornell NanoScale Facility Research Experience for Undergraduates (CNF REU) Program

Principal Investigator(s): James C. M. Hwang; Department of Materials Science and Engineering, Cornell University

Mentor(s): Jin Hong Joo

Primary Source(s) of Research Funding: SUPREME

Contact: jch263@cornell.edu, jj593@cornell.edu, ad.chembravattom@ufl.edu

Summer Program Website(s): https://www.cnf.cornell.edu/education/reu

Primary CNF Tools Used: SUSS MA6-BA6 Contact Aligner, AJA Sputter Deposition, UNAXIS 770 Deep Silicon Etcher, Veeco Savannah ALD, ReynoldsTech Cu ECD Hood, DC Probe Station, Microwave Small-Signal Probe Station

Abstract:

As the demand for heterogeneous-integrated RF chips increases, interposers for millimeter-wave circuits using through-silicon vias (TSVs) have become increasingly important due to their low loss and high-power capacity even at extremely high frequencies. For frequencies above 110 GHz, substrate-integrated waveguides (SIWs) are small enough to be integrated in Si interposers for high-power interconnects.

They can also be used to form high-quality passive devices such as filters and antennas, which have been difficult to integrate on-chip. This enables system-on-chip. In this study, we investigate the fabrication of SIWs and grounded coplanar waveguides (GCPWs) in Si interposers with a thickness of around 200 µm with resistivities ranging from 10-10000 Ω·cm. Thin Si wafers were patterned and etched using the Bosch deep reactive ion etching (DRIE) process to create TSVs. The TSVs were then metallized with platinum (Pt) using atomic layer deposition (ALD) and filled with copper (Cu) using electroplating deposition, before patterning the frontside.

DC measurements confirm a TSV series resistance of less than 1Ω. Small-signal millimeter-wave-on-wafer measurements show that the coplanar interconnects fabricated on high-resistivity (HR, ρ > 1000 Ω·cm) Si have an insertion loss of 0.7 dB/mm at 40 GHz, an order of magnitude better than the same coplanar interconnects fabricated on doped Si (ρ > 10 Ω·cm).

Summary of Research:

Si is the most extensively used material in semiconductor devices due to its exceptional electrical and mechanical properties, including a high dielectric constant, electrical resistivity, breakdown strength, and low loss tangent. These characteristics, and its cost effectiveness, make it an attractive candidate for SIWs. However, its relatively low mechanical toughness and high thermal conductivity compared to materials like silicon carbide (SiC) pose challenges during processing, particularly in etching processes. Our group has previously demonstrated SiC as a viable substrate material for SIW processing, and we adapted the same methodology as a proof of principle for Si SIW fabrication.

To develop a processing recipe for Si-based SIWs, we used a thinned HR Si wafer with a thickness of approximately 200 µm and resistivity greater than 1000 Ω·cm. Building on a similar methodology used for SiC SIWs while taking advantage of the more advanced etching processes available for Si, we began by depositing a 50 nm layer of aluminum oxide (Al2O3) on the wafer's backside using AJA Sputter deposition. Al2O3 was selected as the etch mask due to its excellent masking performance in the Bosch DRIE process for Si, providing a high selectivity greater than 1:1000.

The DRIE was performed using the UNAXIS 770 Deep Silicon Etcher. The etching chemistry employed C4F8 and SF6, which react with Si to anisotropically form vias. As shown in Figure 1, this process yielded 200 µm-deep TSVs with a diameter of 50 µm and sidewall angles ranging from 80 to 90 degrees.

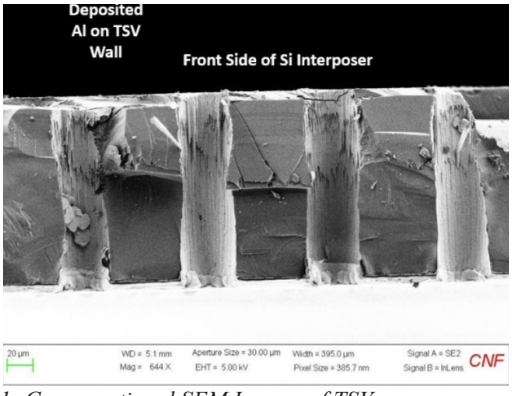

Figure 1: Cross-sectional SEM Images of TSVs.

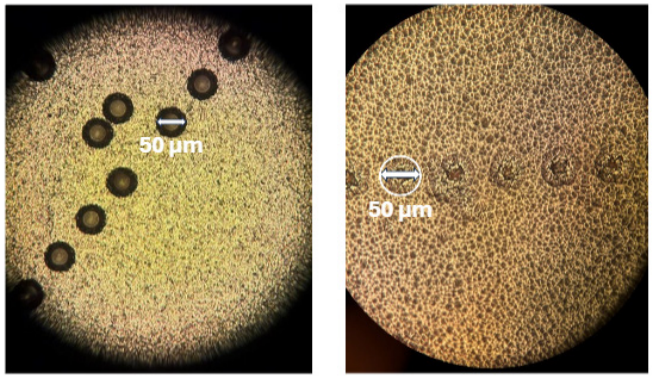

Figure 2: Top-View Optical Image of TSVs After 3 and 12 Hours of Cu Electroplating.

After the TSVs were fully etched through, ALD was used to coat the TSV sidewalls with a Pt seed layer, functioning also as an effective diffusion barrier and adhesion layer. Cu was then electroplated to fill the TSVs, initiating from the Pt seed layer, as illustrated in Figure 2.

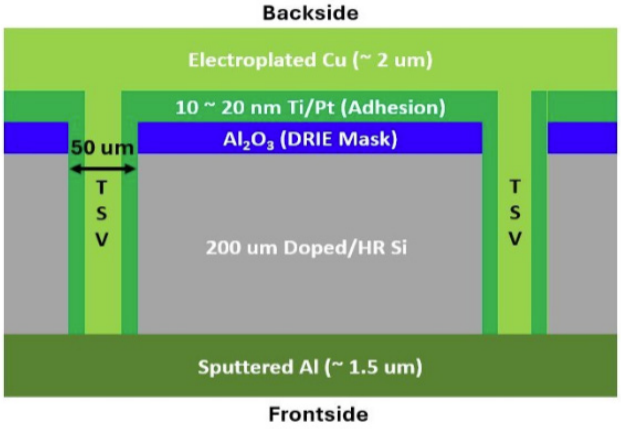

Figure 3: Schematic of Si Interposer Layout.

Once the backside processing was completed, the front side was patterned with SIW and GCPW lines. A platinum/aluminum (Pt/Al) layer was subsequently deposited using AJA Sputter deposition to complete the vertical interposer pathway. The structural details and final device configuration is depicted in Figure 3.

Both HR and doped Si devices were tested at the High Frequency Test Lab (HFTL) where TSV series resistance and GCPW line performance were evaluated. Using the DC probe station, I-V measurements showed that the TSV series resistance was typically below 1Ω for both HR and doped Si substrates. I-V curves also confirmed a resistivity ranging from 4.7 to 17.4 kΩ·cm, confirming that high resistivity of the HR Si substrate. RF measurements were then conducted over the 1-40 GHz range using the small-signal probe station, as shown in Figure 4.

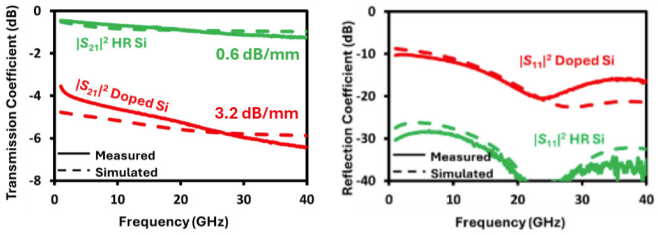

Figure 4: Measured Insertion Loss (S21) and Return Loss (S11) of Doped and HR Si Substrates Across 1-40 GHz.

For HR Si, the insertion loss (S21) value was approximately 0.7 dB/mm, with return loss (S11) exceeding 20 dB. In comparison, doped Si devices exhibited a much higher insertion loss of approximately 3.2 dB/mm and a return loss greater than 10 dB.

Conclusions and Future Steps:

The fabrication of Si interposers focused on optimizing Bosch DRIE of thinned Si wafers and refining metallization processes to achieve uniform anisotropic etching and consistent metal filling across the wafer. Measurements comparing HR and doped Si substrates revealed that HR Si shows insertion losses an order of magnitude lower than the doped Si, highlighting its potential as a promising substrate material for millimeter-wave applications. Looking ahead, with updated tools and improved techniques for etching and metallization, fully metal-filled TSVs are expected to achieve insertion losses below 0.5 dB/mm at frequencies up to 220 GHz, utilizing the 220 GHz single-sweep probe station at HFTL; once these targets are achieved, our group hopes to achieve heterogeneous integration in the cleanroom with flip chip bonding.

References:

[1] M. J. Asadi, L. Li, K. Nomoto, Y. Tang, W. Zhao, P. Fay, D. Jena, H. G. Xing, and J. C. M. Hwang, "SiC Substrate Integrated Waveguides for High-Power Monolithic Integrated Circuits Above 110 GHz," 2021 IEEE MTT-S Int. Microw. Symp. (IMS), Atlanta, GA, USA, 2021, pp. 669–672.

[2] D. Malta, E. Vick, S. Goodwin, C. Gregory, M. Lueck, A. Huffman, and D. Temple, "Fabrication of TSV-based silicon interposers," 2010 IEEE International 3D Systems Integration Conference (3DIC), Munich, Germany, 2010, pp. 1–6.

[3] M. Leskela and M. Ritala, Thin Solid Films 409, 138 (2002).

[3] F. Laermer et al., IEEE Microelectromech. Syst. 211 (1999).

Characterization of PFAS Free PAGs in Photoresist

CNF Intern: Landon Cheung
Student Affiliation: Tompkins Cortland Community College (TC3)

Summer Program(s): 2026 Cornell NanoScale Facility Summer Internship
Mentor(s): Chris Ober, Professor Zhong, Sherri Ellis

Primary Source(s) of Research Funding: NORDTECH

Contact: 75lcheung@gmail.com, cko3@cornell.edu, see43@cornell.edu

Summer Program Website(s): https://www.cnf.cornell.edu/education/reu

Abstract:

The reduction of PFAS 'forever chemicals' has been of recent focus for the semiconductor industry for both legislative and environmental concerns. These chemicals, containing -CF2- or -CF3 bonds1, are difficult to break down due to high bond energy and thermal stability. PFASs are of concern to the environment due to this property, building up in the biosphere and interfering with biological systems. Recent legislation is pushing for the removal of PFASs in the semiconductor industry leading to the need for PFAS free photoresists2. This project focuses on the performance of PFAS-free PAGs in photosensitive resists, which may match or outperform their PFAS counterparts and factors that influence it.

Summary of Research:

Photosensitive resists generally have four steps: pre-bake, exposure, post exposure bake (PEB), and development. In the baking stages, temperature and time affect the results and properties. Exposure is influenced by dosage, mJ or uC/cm^2, given to the photoresist and correlates with resist thickness. Overexposure also poses a concern with cross-linking, causing the photoresist to become insoluble and harder to remove than an adequately exposed area. Proper development ensures that the exposed or unexposed sections, depending on whether a positive or negative resist is utilized, dissolve completely.

One of the tests uses a PFAS free PAG-bound ESCAP resist with an array of resolution tests that varied the dose using the ASML 5500 DUV stepper. The stepper is capable of resolution down to 200 nm, setting the best possible result. The criteria for a good resist are development through the thickness of the resist and smooth edges that follow the original pattern. However, due to effects such as corner rounding, optical diffusion, acid diffusion, and optical proximity effects, small features will have more pronounced rounding and imperfections when compared to the original mask.

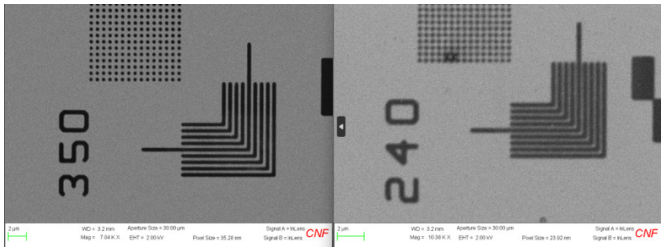

Figure 1: DUV resolution comparison at 350 nm and 240 nm.

Figure 1 compares a good result in a DUV in the bulk of the feature at 350 nm, compared to expanded lines on 240 nm. The rounded corners and ends of the lines test show the optical and chemical effects of photolithography. Figure 2 has good features at 300 nm and continually decreases in quality down to 250 nm. 300 nm has clear edges with some variations, overall a good result. 280 nm has noticeably less quality, with more jagged edges and some sections bridging on the sides. Under 280 nm is unviable, having too much inconsistency.

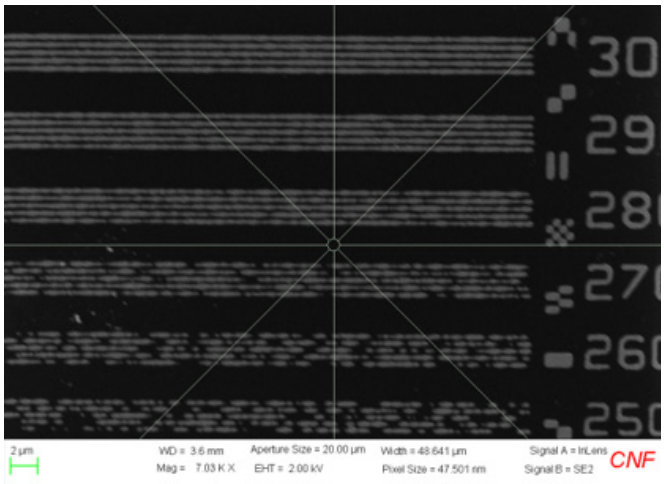

Figure 2: DUV resolution test at approximately 115.5 mJ/cm^2 with good results at the top starting at 300 nm and getting worse as you go down to 250 nm..

E-beam photoresists were tested in lieu of EUV due to the mechanism of how EUV PAG resists work. They rely on secondary electrons to create an acid that allows for the photomask to become more soluble. Using the Nabity NPGS and Zeiss Supra SEM, the electron beam skips to the secondary electron state, bypassing the need for EUV radiation to generate secondary electrons. This was used to test resolution and how thorough the thickness the photoresist exposures are. Using AFM, each dose's height map is recorded then digitally processed. Using Gwyddion, the major steps are background slope removal, averaging the depth of the exposure development, and normalizing using the thickness of the resist (fig. 3). This gives us the exposure thickness of the resist. The P3 PAG (fig. 4) was tested, with the best resolution of the set at 500 nm (fig. 3).

Conclusions and Future Steps:

This research shows room for improvement for using PFAS-free PAGs, with up to 90 nm of improvement potential for DUV on the ASML 5500. The main limitation with testing is how fast the PAGs can be synthesized, with only enough being made for one or two samples per week. These characterizations show a significant step in moving toward PFAS-free photoresists by utilizing PFAS-free PAGs. However, more testing and improvements to the process are needed before they can be applied and reduce PFASs in the environment.

References:

[1] OECD (2021), Reconciling Terminology of the Universe of Per- and Polyfluoroalkyl Substances: Recommendations and Practical Guidance, OECD Series on Risk Management of Chemicals, OECD Publishing, Paris, https://doi.org/10.178

[2]. Environmental Protection Agency. (2019). EPA PFAS action plan (EPA 823-R-18-004). U.S. Environmental Protection Agency. epa.gov

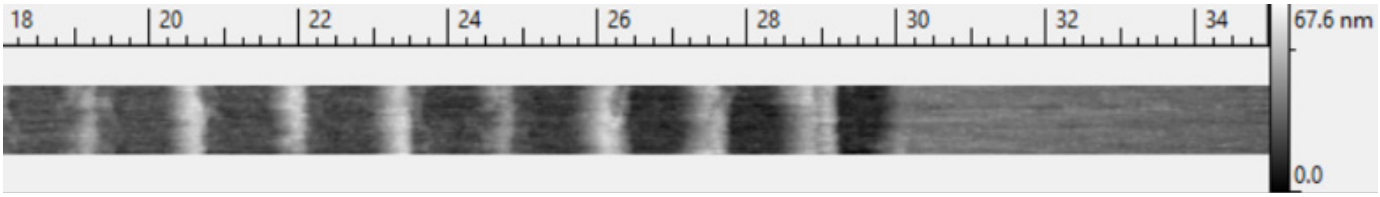

Figure 3: Ebeam resolution test with 500 nm line distance and width. Dose of 125 uC/cm^2 for the tested setup of 110°C for 240s.

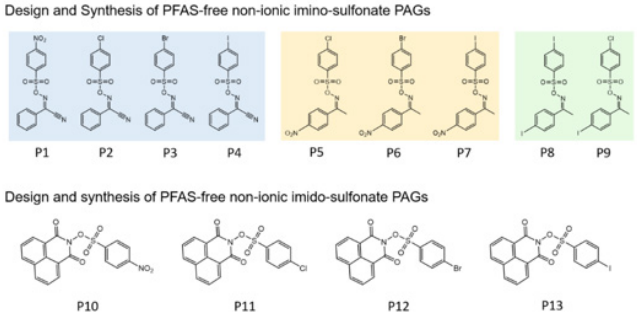

Figure 4: PFAS free PAG chemicals. Report on identification of PFAS-free non-ionic PAGs as solubility switch groups in photoresists. Task #: 3244.001. Christopher K. Ober, Yu Zhong.

Characterizing Downstream Mechanisms of *LMNA*-Associated Dilated Cardiomyopathy Using a Myocardial Tissue-Slice Model

CNF Summer Student: Andrew Diviney
Student Affiliation: Meinig School of Biomedical Engineering, Cornell University

Summer Program(s): 2026 Cornell Cardiac Undergraduate Research Experience (CURE)

Principal Investigator(s): Jan Lammerding

Mentor(s): Julie Heffler

Primary Source(s) of Research Funding: American Heart Association

Contact: akd88@cornell.edu, jan.lammerding@cornell.edu, jh2347@cornell.edu

Summer Program Website(s): https://www.cnf.cornell.edu/education/reu

Abstract:

LMNA-associated dilated cardiomyopathy (LMNA-DCM) is a genetic cardiac disease caused by mutations in the LMNA gene, which encodes the nuclear envelope proteins lamin A/C. Although LMNA mutations are known to disrupt nuclear structure and mechanotransduction, the downstream mechanisms connecting these defects to cardiac dysfunction remain poorly understood. A common hallmark of LMNA-DCM are misshapen or damaged nuclei, which we hypothesize drives disease pathology. Nuclear damage causes the release of nuclear content, exposure of DNA to the cytoplasm, DNA damage, and cellular stress through a myriad of pathways, but we do not know which specific pathways drive disease progression, if any.

We hypothesize that nuclear envelope damage causes sarcoplasmic reticulum (SR) stress, altering calcium handling and protein homeostasis. Initial experiments investigated the response of isolated cardiomyocytes to SR stress using thapsigargin and tunicamycin. However, a three-hour treatment period was insufficient to produce a robust stress response, highlighting the limited experimental window of isolated cardiomyocytes. To address this limitation, we developed a murine myocardial tissue-slice model that preserves native cardiac environment and cellular interactions while allowing tissue to remain viable for longer periods. This model provides a platform for longer term imaging and controlled stimulation, enabling investigation of disease mechanisms over time. Future studies will use the model to examine calcium dynamics and stress responses in LMNA-mutant tissue and determine whether altered calcium handling and SR stress contribute to LMNA-DCM progression.

Summary of Research:

To investigate potential downstream effects of LMNA-associated cardiomyopathy, we first examined whether inducing SR stress in isolated cardiomyocytes was sufficient to induce pathways previously identified in a transcriptomics study. Wild-type cardiomyocytes were treated with the SR stress-inducing compounds thapsigargin (5 μM) and tunicamycin (5 μM or 10 μM) for three hours, and changes in ER/SR-associated proteins were measured. While the experiment provided an initial indication that SR stress may affect protein expression, the three-hour treatment did not produce a strong enough response to draw definitive conclusions.

This result highlighted an important limitation of the isolated-cell approach. Three hours may not be long enough for downstream changes in protein expression and calcium handling to develop. At the same time, substantially extending the treatment could cause excessive cellular stress and cell death. Isolated cardiomyocytes have a limited lifespan and lose many of the structural and cell-cell interactions present in intact cardiac tissue. Together, these limitations make it difficult to study processes that develop over longer timescales.

To address this, we developed a myocardial tissue-slice model that allows cardiac tissue to be maintained in culture for up to 48 hours while preserving its native architecture. Thin sections (250 μm) of mouse myocardium retain cardiomyocytes and surrounding heterogeneous cellular interactions and extracellular matrix structures, providing a more physiologically relevant environment than isolated cells.

We developed a 3D printed custom mounting system to hold the myocardial slices during culture and imaging. The three-part mounting system is designed to keep the tissue under constant tension, and the addition of electrical pacing lets us mimic the electrical and mechanical environment of the heart. We developed a pacing device to provide electric stimulation to the tissue. The pacing device consists of a 3D printed lid to

a 6 well plate that allows us to hang graphite electrodes down into the tissue media. Because the electrodes need to be extremely conductive but not affect the tissue sample, we coated the graphite in PEDOT:PSS, 5% v/v DMSO, and 1% GOPS. The combination of these chemicals prevents particles from dissociating into the media while retaining maximum conductivity. This platform will allow us to move beyond short, endpoint experiments and instead monitor changes in cardiac tissue longitudinally.

This model directly addresses the limitations of the initial three-hour experiment. Instead of exposing isolated cardiomyocytes to prolonged stress until they lose viability, the tissue-slice system provides a longer experimental window in which we can monitor how cardiac tissue responds to SR stress. This will allow us to determine whether changes that were not detectable after three hours emerge following longer treatment and whether those changes differ between WT and LMNA-mutant tissue.

Ultimately, the model provides a foundation for studying calcium dynamics, cellular stress responses, and disease progression longitudinally in a more native cardiac environment.

Conclusions and Future Steps:

The initial SR-stress experiments demonstrated the limitations of using isolated cardiomyocytes for studying processes that may require longer periods in culture. Rather than treating this limitation as an endpoint, we developed a myocardial tissue-slice model designed to provide a longer experimental window while preserving native cardiac structure and cellular interactions.

The resulting platform establishes a foundation for longitudinal studies of LMNA-DCM. Future work will first optimize tissue-slice culture and imaging conditions to establish consistent tissue viability and measurements over time. We will then perform longer SR-stress experiments to determine whether prolonged treatment produces measurable changes in stress-response pathways and calcium handling.

Future experiments will use Fluo-4 calcium imaging to compare calcium dynamics between WT and LMNA-mutant tissue. Additional markers of ER stress, including phospho-PERK, will help determine whether prolonged SR stress activates cellular stress pathways. The model can also be used to investigate how mechanical stimulation influences these responses.

Ultimately, the goal is to use this platform to determine whether altered calcium handling and SR stress are downstream consequences of LMNA-associated nuclear dysfunction and whether these changes contribute to the progression of LMNA-DCM. By enabling longer-term observation in a more native cardiac environment, the myocardial tissue-slice model provides a new approach for studying disease mechanisms that cannot be adequately captured using short-term experiments in isolated cardiomyocytes.

Acknowledgments:

Thank you to the Cornell Cardiac Undergraduate Research Experience (CURE) program funded by the National Science Foundation (NSF) and American Heart Association (AHA), and a special thank you to the Lammerding Lab, especially my advisor, Dr. Jan Lammerding, and my mentor, Dr. Julie Heffler.

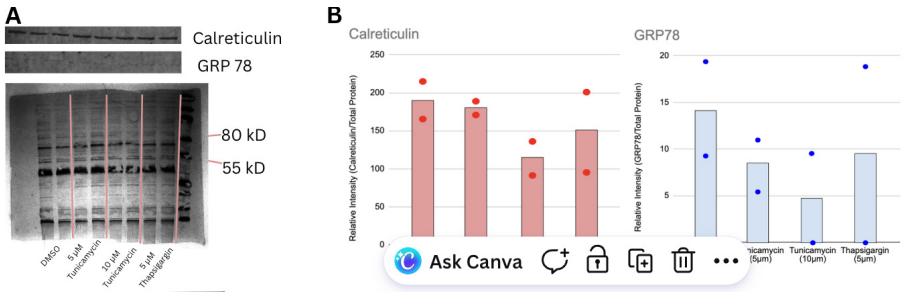

Figure 1: (A) Representative Western blot, proteins of interest on top, total protein below. (B) Analysis showing decreases in calreticulin (left) and GRP78 (right) with higher concentrations of positive control SR stress drugs Tunicamycin and Thapsigargin. Note that all cells treated with 10µM Thapsigargin died before the 3 hour treatment period ended.

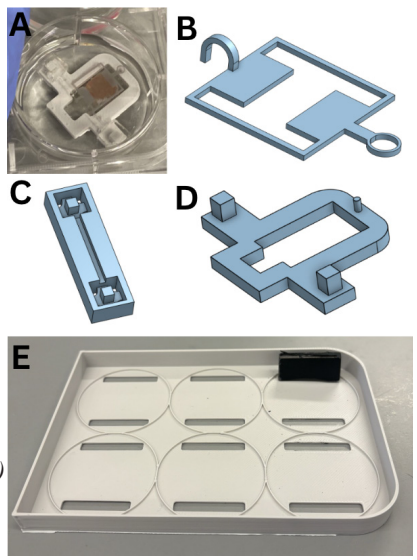

Figure 2: A) Sample loaded into the full device in a 6 well plate. (B) 3D rendering of the tissue mount. (C) 3D rendering of mold used to cast the tissue stretching band. Use 1:10 PDMS to get correct tensile strength. (D) 3D rendering of the base design used to hold the band and keep the mount level for imaging. (E) 3D printed lid for 6 plate well that allows electrodes to hang down into the media. Graphite electrodes are coated in PEDOT:PSS (a highly conductive polymer) with 1% m/v GOPS and 5% v/v DMSO to prevent graphite particles from breaking off into the media.

iCVD Polymer Microparticle Synthesis Inside a New Liquid Crystal

CNF Summer Student: David Eastman
Student Affiliation: Department of Chemistry, Biochemistry, and Physics, Indiana University of Pennsylvania

Summer Program(s): 2026 Cornell NanoScale Facility Research Experience for Undergraduates (CNF REU) Program
Principal Investigator(s): Dr. Nicholas Abbott and Dr. Rong Yang; R.F. Smith School of Chemical Engineering, Cornell University
Mentor(s): Soumyamouli Pal, Shiqi Li
Primary Source(s) of Research Funding: NSF Future Manufacturing Research Grant (FMRG) Grant No. NNCI-2025233
Contact: nla34@cornell.edu , ryang@cornell.edu, jqkfc@iup.edu
Summer Program Website(s):
Research Group Website: https://nlabbottcornell.weebly.com/, https://theyanglab.com/
Primary CNF Tools Used: AJA3 Sputtering Tool, Zeiss Ultra 55 SEM

Abstract:

Liquid crystals (LCs) can be used as templates to influence polymer morphology during initiated chemical vapor deposition (iCVD). In this study, the liquid crystal TL205 was investigated as a new templating material and compared with the commonly used liquid crystal E7. Polymer was deposited using iCVD under varying deposition parameters, and the resulting morphologies were characterized to determine how polymer growth differed between the two LC templates. Differences in morphology were observed as a function of deposition conditions and LC template, demonstrating that the choice of liquid crystal can influence the resulting polymer structure. To investigate a potential explanation for these differences, the solubility of the monomer in TL205 and E7 was evaluated. The solubility results provide an indication that differences in monomer-LC interactions may contribute to the observed morphological behavior. However, more characterization and experiments are needed to fully determine what is responsible for the differences between TL205 and E7 polymer

Summary of Research:

Liquid crystals are materials that have properties of both liquids and crystalline solids. Although they are able to flow like a liquid, their molecules maintain a degree of orientational order. This combination of fluidity and molecular organization makes liquid crystals useful as environments for controlling polymer growth. The molecular organization and chemical properties of a liquid crystal can influence how a polymer forms inside of it. Factors such as monomer solubility, molecular interactions, and viscosity can affect polymer nucleation, growth, particle size, and morphology. Therefore, changing the liquid crystal could result in changes to resulting polymer particle size, morphology, etc. [1] [2]

Initiated Chemical Vapor Deposition (iCVD) is a solvent-free technique that can be used to synthesize polymers into the liquid crystal. During iCVD, a monomer, divinylbenzene (DVB) and initiator, tert-butyl peroxide (TBPO), are introduced into the chamber, where a heated filament breaks the initiator, into free radicals that initiate polymerization. Because process parameters such as filament temperature, chamber pressure, flow rates, and deposition time can be controlled independently, iCVD provides a useful method for investigating how different process parameters affect polymer formation. [1] The iCVD reactor setup is shown in figure 1.

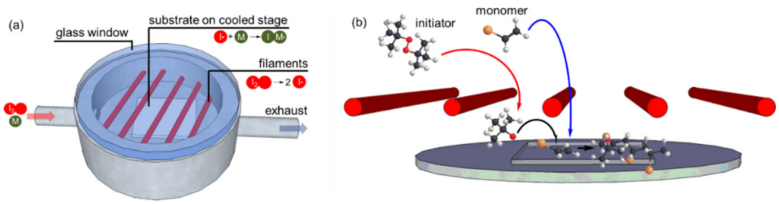

Figure 1: iCVD Reactor Setup.

In this study, a novel and fluorinated liquid crystal, TL205 (TNI=87-90°C), was investigated as a template for polymer growth, and compared to a standard and well investigated liquid crystal, E7 (TNI=60-63). The goal was to determine how the choice of liquid crystal affects the resulting polymer formations. Experiments using a variety of iCVD parameters revealed a difference in

polymer particle size and morphology between the two liquid crystal templates. After establishing that these findings were consistent among a wide range of process parameters, further experiments were conducted to find the reason for these differences. A solubility test was done to determine if the reason for the different polymer particle sizes and morphologies is due to a difference in concentration of monomer in the different liquid crystals. This study provides insight into how different liquid crystals behave as a template for polymer growth during iCVD.

Experiments were completed with varying filament temperature, initiator/monomer flow rate ratio, and deposition time. In one experiment that gave particularly clear results, the filament was heated to ≈300°C, a high initiator/monomer ratio of 0.7 was used, and a featured deposition time of 120 minutes. In figure 2, the resulting polymer formation when an E7 template was used can be seen. The polymer particles, which are roughly 1.7 µm in diameter, are arranged in an energetically favorable hexagonal array. Qualitatively, the array is ordered, and particles are roughly uniform in size. In figure 3, the resulting polymer formation when a TL205 template was used can be seen. In contrast to when E7 was used, the polymer morphology contains a mixture of hexagonally ordered particles, stray particles, and large clusters of aggregated polymer. The particles were found to be notably smaller, with an average particle size of ≈1.3 µm. All quantitative analysis of particles was performed using ImageJ/Fiji, and the "Analyze Particle" Function.

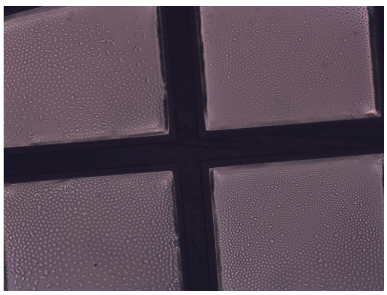

Figure 2: Resulting polymer formation when E7 was used as a template for polymer growth. Neat hexagonal array of polymer particles.

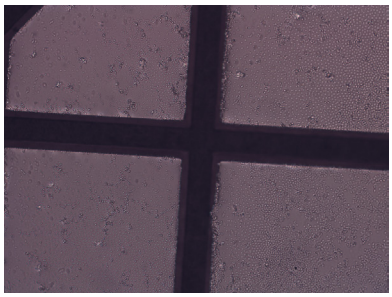

Figure 3: Resulting polymer formation when TL205 was used as a template for polymer growth. Less ordered array of polymer particles. Polymer clusters can also be seen.

To confirm results, iCVD was repeated with varying parameters, such as filament temperature, initiator/monomer ratio, and deposition time. In every trial, the same pattern emerged: When TL205 is used as a template for polymer growth, the result is smaller polymer particles as well as a much less ordered arrangement of particles. Since this pattern is consistent across many varying parameters, the cause for these differences was investigated. Given the fluorinated nature of TL205, it was hypothesized that the monomer, DVB, is less compatible with the TL205 than E7 and there is likely a lower concentration of DVB in TL205 than E7, which would result in smaller particles in TL205 as well as decreased order. This was tested through a two-part solubility test that relies in Henry's Law, meaning that the pressure of monomer above the liquid crystal is directly proportional to the concentration of monomer inside the liquid crystal. The conclusion of this study revealed that contrary to the hypothesis, there is a higher concentration of DVB in TL205 than E7. Given the specific parameters of the depositions used in this study, the concentration of DVB in TL205 is 0.429 M, while the concentration is only 0.301 M in E7. While monomer solubility certainly affects polymer formations, more testing needs to be done to determine the cause for the decreased particle size and disorder that is seen when TL205 is used as a template for growth.

Conclusions and Future Steps:

When TL205 is used as a template for polymer growth, smaller polymer particles are formed, and formations are generally more clustered and chaotic than when E7 is used as a template for polymer growth. The reason for this is not due to increased monomer solubility in E7 compared to TL205 as we hypothesized, and more testing of LCs needs to be done to determine the reason for the differences in polymer morphology.

Concentrations with my deposition conditions	E7	TL205
Concentration of DVB in LC	0.301 M	0.429 M

Figure 4: Results of solubility test.

References:

[1] Jain, A et al., Single-step synthesis of shaped polymeric particles using initiated chemical vapor deposition in liquid crystals. Sci. Adv 2024 10, eadp5573. DOI:10.1126/sciadv.adp5573.

[2] Angew. Chem. Int. Ed. 2025, 64, e202015703 doi.org/10.1002/anie.202515703.

[3] Research – The Yang Lab. (2026). Theyanglab.Com. https://theyanglab.com/research/.

Metal-Oxide Interface Preservation Using Atomic Layer Deposited Metal Interlayers

CNF Summer Student: Lincoln Hogan
Student Affiliation: Department of Electrical and Computer Engineering, North Carolina State University

Summer Program(s): 2026 Cornell NanoScale Facility Research Experience for Undergraduates (CNF REU) Program

Principal Investigator(s): Grace Xing, Cornell University

Mentor(s): Joseph Dill

Primary Source(s) of Research Funding: NSF SUPREME REU

Contact: ldhogan@ncsu.edu, grace.xing@cornell.edu, jed296@cornell.edu

Summer Program Website(s): https://www.cnf.cornell.edu/education/reu

Abstract:

Energetic metal deposition techniques have been shown to introduce defects at the metal–oxide (MO) interface, degrading the electrical performance of gate dielectrics in MOS structures. In this work, we compare MO interface degradation resulting from conventional energetic metallization techniques with that of atomic layer deposited (ALD) gate metals. We demonstrate that fully in-situ ALD dielectric and metal deposition provides minimal improvement over post-passivation ALD metallization, indicating that air exposure following ALD passivation does not significantly degrade interface quality. Finally, we show that thin ALD gate metals preserve the MO interface during subsequent energetic metal deposition, enabling additional metallization without measurable degradation of dielectric performance. These results demonstrate that thin ALD metal interlayers provide an effective strategy for preserving MO interface quality while maintaining flexibility in subsequent metallization processes and material selection.

Summary of Research:

Energetic Physical Vapor Deposition (PVD) gate metallizations have been shown to degrade dielectric quality through the introduction of defect states [1]. X-Ray and UV radiation from Magnetron Sputtering and Electron-Beam Evaporation (EBE) can break dielectric bonds. Argon ions from Sputter plasma embed themselves deep in the dielectric [1]. According to the Multiphonon Trap Assisted Tunnelling (TAT) theory, Fowler-Nordheim (FN) TAT is maximized when defect states lie 29.3% of the tunnelling barrier distance away from the cathode (x*) [2], [3]. Interface trap states can also increase TAT by lowering the effective barrier at the Metal-Oxide (MO) interface (ΦMO) as seen in Fig. 1. Higher initial tunnelling current (I0) results in earlier time-to-breakdown (tBD) due to a higher population of lucky electrons as shown in Fig. 2 [2]. This means that the more penetrative the deposition is, the faster the device will break.

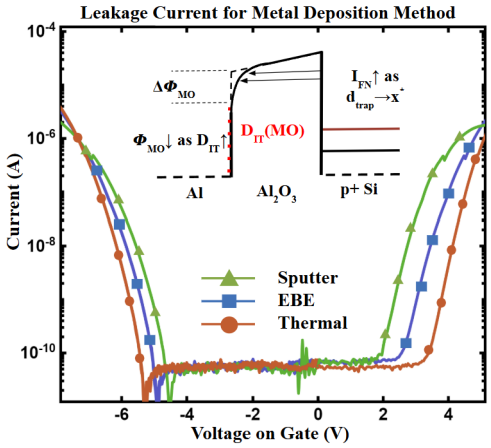

Figure 1: I-V sweeps on 180 μm DIA pads on 15 nm Al_2O_3. Traps at the MO interface lower the effective barrier ΦMO. Sputtering results in the earliest onset current due to high DIT (- bias) and deep dtrap (+ bias).

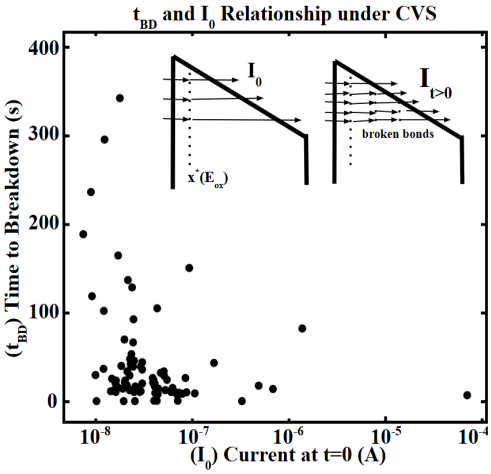

Figure 2: Time-to-breakdown is plotted against initial leakage current at constant voltage stress (CVS). It is shown that higher tBD is achieved when I0 is low. High defect density at x results in maximized I0.*

CNF REU

We fabricate nine Al/Al_2O_3/p+Si MOS capacitors with varied metallization methods. C-V measurements show oxide capacitance (Cox) remains comparable between the samples, indicating Al_2O_3 thickness and dielectric constant (εox) are unchanged. In Fig. 1 our I-V plot confirms literature reports that Sputtering results in the earliest onset TAT, followed by EBE and Thermal Evaporation [1]. Positive bias likely represents increased FN current due to barrier lowering, while negative bias likely indicates trap-limited Frenkel-Poole (FP) tunnelling. Three Thermally Evaporated samples are produced with 30, 15, and 5 nm oxides to access thickness dependence. C-V measurements confirm a plausible Density of Interface Traps (DIT) and Cox thickness trend, J-E leakage plots showed no dependence on thickness, further indicating that leakage through the Al_2O_3 is largely governed by interfacial defects.

After the energetic PVD study we fabricate TiNx/Al_2O_3/p+Si MOS capacitors with ALD metallization. J-E plots showed almost 2x increase in negative bias TAT onset field for ALD metallization compared to Thermal. The 0.5 eV increase in ΦMO from Al to TiNx is not relevant to our J-E negative sweeps which are largely dominated by trap-limited FP tunnelling. FN tunnelling still occurs, but the tunnelling barrier is too thick for ΦMO to be rate-limiting. Time-dependent dielectric breakdown (TDDB) measurements under constant voltage stress (CVS) in Fig. 3 confirm that ALD metallization yields higher tBD when compared to Thermal. This likely arises from the significantly lower leakage current I0 in the ALD sample [2].

Despite its proven advantages, the cost, processing time, and material limitations of ALD have hindered its widespread adoption as a gate metallization technique. We demonstrate that integrating a thin ALD metallization layer between dielectric deposition and conventional PVD metallization enables broader process compatibility while preserving MO interface integrity. We compare EBE Cr (150nm) deposited on TiNx (40 nm) and Al_2O_3 (7 nm) ALD films grown under vacuum with an identical film that was exposed to atmosphere between Al_2O_3 and TiNx. We additionally compare a vacuum-deposited TiNx/Al_2O_3 film with no EBE Cr. Weibull analysis in Fig. 4 reveals no variation in tBD or Weibull slope (β) between the three samples. Additionally, negative field J-E sweeps appear consistent across samples. From this analysis we can infer that the MO interface is protected from EBE by 40 nm TiNx and oxygen defects at the MO surface have little impact on tunnelling current. This follows our earlier framework, as oxygen defects are significantly shallower than x* [3].

In this work we demonstrate dielectric quality degradation across various energetic PVD methods [1] and compare an example of ALD metallization. We have shown that 40 nm TiNx can be deposited on Al_2O_3 after air-transfer and prior to EBE of Cr while still preserving the metal-oxide interface. This work establishes the foundation for ALD interlayer engineering. Future studies should determine the minimum effective interlayer thickness and evaluate compatibility with a broader range of metallization schemes, ultimately enabling a universal metal–oxide interface protection layer.

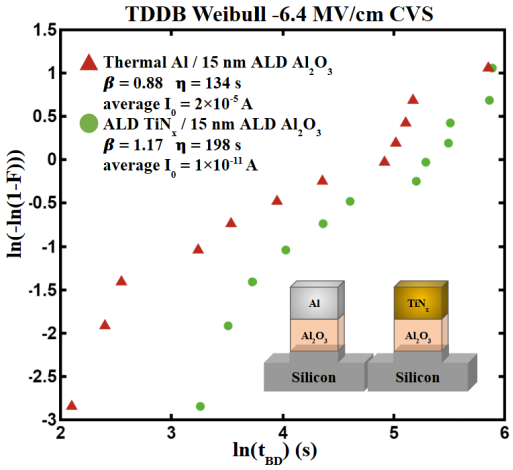

Figure 3: TDDB under CVS at -6.4MV/cm (~90% of EBD). Weibull slope (β) was poor but comparable between samples. The intrinsic time-to-breakdown lifetime (η) increased 47% from Thermal to ALD, while early breakdown times increased almost 177%. We observe 6 orders of magnitude decrease in current at t = 0 from Thermal to ALD.

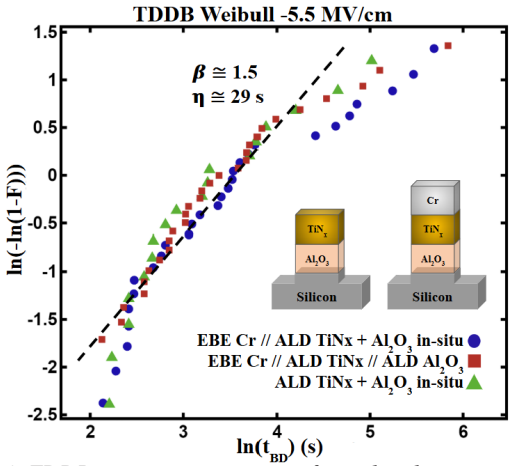

Figure 4: TDDB measurements are performed under constant voltage stress (CVS) at -5.5MV/cm (~90% of EBD). Weibull slope (β) and intrinsic time-to-breakdown lifetime (η) remain consistent across each sample. No change in leakage I0 was observed.

References:

[1] I. Mack et al., "Quantifying the Impact of Al Deposition Method on Underlying Al2O3/Si Interface Quality," Phys. Status Solidi.

[2] Z. Chbili et al., "Modeling Early Breakdown Failures of Gate Oxide in SiC Power MOSFETs," IEEE Trans. Electron Devices.

[3] S. Makram-Ebeid and M. Lannoo, "Quantum Model for Phonon-Assisted Tunnel Ionization of Deep Levels in a Semiconductor," Phys. Rev.

Diamond CVD, NanoBOND/DEBOND System, and Furnace Characterization

CNF Intern: Alexander J. Infante
Student Affiliation: Department of Electrical and Microelectronic Engineering, Rochester Institute of Technology (RIT)

Summer Program(s): 2026 Cornell NanoScale Facility Summer Internship

Mentor(s): Philip Infante, CNF

Primary Source(s) of Research Funding: NORDTECH

Contact: infante.6.ai@gmail.com, pi12@cornell.edu

Summer Program Website(s): https://www.cnf.cornell.edu/education/reu

Primary CNF Tools Used: MOS Clean Bench & Tanks, MRL E2 CMOS Wet Oxide, MRL B3 LPCVD LTO, Woollam RC2 Spectroscopic Ellipsometer, Filmetrics F50, Bruker DektakXT Profilometer, Zeiss Gemini SEM, Zeiss Ultra SEM, Keyence VHX-7100 Digital Microscope, NanoBOND 200, NanoDEBOND 200

Abstract:

Summer project goals included work on the Nordtech funded Seki Diamond chemical vapor deposition tool and the Nordtech funded OnNano NanoBOND 200 and NanoDEBOND 200 system. The goal with the Seki Diamond tool was to characterize and perform a hardware assessment of the tool. The work completed on that project was the development of a nanodiamond seed crystal coating process, essential for serving as a nucleation point for diamond chemical vapor deposition. Project time was limited when the tool was shut down for repair. This caused a pivot to the NanoBOND 200 and NanoDEBOND 200 system. The task was to perform a hardware assessment of the system and develop processes for operation, with the ultimate goal being a complete operating manual.

Summary of Research:

Nanodiamond Seed Crystal Process

The Seki Diamond tool functions by using a microwave plasma, 99% Hydrogen and 1% methane. In the plasma is a diamond seed crystal which the methane will contact, depositing its carbon atom onto the diamond lattice structure. The remaining hydrogen in the methane molecule will join the existing hydrogen plasma cloud. This reaction builds a layer of diamond, atom at a time on top of a diamond seed crystal. The reaction will only grow diamond on diamond. For this purpose, it is essential to the process that we have proper diamond seed crystals for diamond chemical vapor deposition.

The Seki Diamond tool uses a molybdenum puck as its base for seed crystals. Seed crystals can either be monocrystalline, one large diamond with a singular lattice direction, or polycrystalline, many smaller diamonds with various lattice directions. To initially characterize the diamond growth rate, polycrystalline seeds were preferred for their much lower cost. The seed crystals are roughly 20nm in diameter, requiring a scanning electron microscope for imaging. This factor meant the original molybdenum puck would have a surface too rough to observe any seed crystal deposition. Instead, two-inch silicon wafers were preferred for their availability and smooth surface, even though they will never be used in the Seki Diamond tool. A ScienceDirect article recommended starting with a 50% dimethyl sulfoxide (DMSO) diamond solution to 50% methanol. A two-inch wafer was placed in this 50/50 solution and moved into an ultrasonic bath for 10 minutes, after the bath wafers were rinsed with more methanol and dried with nitrogen [1]. When this recipe was observed under the Zeiss Gemini SEM560 scanning electron microscope, many of the diamonds had collected into water spots and were not evenly dispersed across the wafer. To solve this the process was modified to see if a lower concentration, different cleaning method, and different sonication times, improved results. The ideal recipe found was a 25%/75% DMSO to methanol solution, sonicated for 15 minutes, and cleaned with isopropanol (Figure 1).

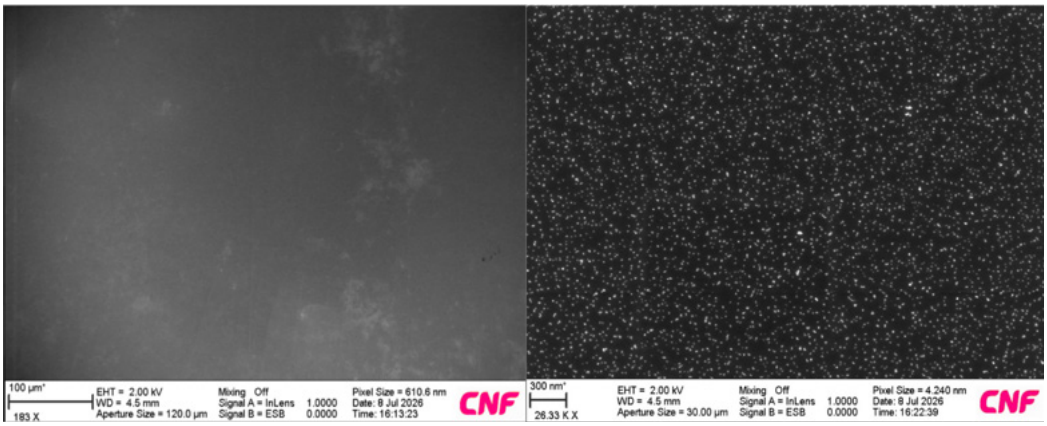

Figure 1: Nanodiamond Seed Crystals. 15 minutes, 25% DMSO, cleaned with IPA.

NanoBOND 200 and NanoDEBOND 200

The hardware assessment for both the NanoBOND 200 and NanoDEBOND 200 involved testing, experimentation, and troubleshooting. The NanoBOND 200 and NanoDEBOND 200 system functions by coating a carrier wafer with a bonding polymer and bonding to either another target wafer or wafer piece. Theoretically the carrier is thicker and stronger than the target, adding structural support as the target undergoes process steps. When the carrier has served its purpose, the bonded stack is then slid apart in the NanoDEBOND 200 tool. Initially much time was devoted to developing a spincoating process for MicroResist, mr-glue-xp bonding polymer. The given process yielded streaking and uneven polymer surfaces. Through trial and error, a two-step spinning recipe was created for the three different carrier wafer sizes, four inch, six inch, and eight inch.

Our operating process had to be adjusted for the original setup of the tool. The NanoBOND 200 has two vacuum chucks, one for the carrier and one for the target, however neither chuck has an included aligning mechanism. To resolve this, a wafer aligner for each chuck was modeled and is being machined. The NanoDEBOND also required other adjustments. One being that during the debond process the carrier is supposed to be held in place on the carrier vacuum chuck not only by vacuum, but by a physical lip impeding the direction of sliding. This lip was measured to be 600 microns thick, 75 microns thicker than a standard four-inch wafer. This led to bonded stacks on four-inch carrier wafers breaking as they hit the lip when debonded. A fix to machine down this lip is on the way. Another critical flaw with the debonder was the lack of any refined wafer removal mechanism. Originally the debonded carrier and target wafers were removed with tweezers or by hand. Since they are oriented vertically and at temperatures over 100 degrees Celsius this is suboptimal. An effective solution was using a vacuum wand to remove the wafers. After the hardware assessment and subsequent solutions, a full manual of operation was made, including all operation steps for spin coating, bonding, and debonding, as well as general information useful for future users.

Furnace Characterization

Additionally, during transition time between projects time was allocated for work on the E2 Wet Oxide furnace and the B3 LPCVD furnace. The goal for the E2 wet oxide was to create a Deal-Grove equation for oxide thickness. This was done using nine trial runs of varying time and temperature. A model was made that can predict thickness with 80% accuracy, which needs more refining before further use. Work on the LPCVD furnace used three runs of 35 wafer batches to measure uniformity across wafer position in the tube. This successfully identified variation is presented in the front of the tube.

References:

[1] Shenderova, O. A., & ScienceDirect. (2010, March). Seeding slurries based on detonation nanodiamond in DMSO. Diamond and Related Materials, Volume 19(2-3), 260-270. https://www.sciencedirect.com/science/article/pii/S0925963509002830

Optimization of Live Bi-Ventricular Slice Culture Platform for Embryonic Ventricular Morphogenesis Investigation

CNF Summer Student: Sanskriti Nanda
Student Affiliation: Department of Biological Sciences, SUNY Oswego

Summer Program(s): 2026 Cornell Cardiac Undergraduate Research Experience (CURE)
Principal Investigator(s): Jonathan Butcher
Primary Source(s) of Research Funding: American Heart Association
Contact: jtb47@cornell.edu, snanda@oswego.edu
Summer Program Website(s): https://www.cnf.cornell.edu/education/reu

Abstract:

Congenital heart defects (CHDs) affect approximately 1 in 100 live births, making understanding embryonic cardiac development essential for identifying mechanisms underlying abnormal ventricular morphogenesis. This project focused on optimizing a live bi-ventricular slice culture platform using Hamburger-Hamilton stage 36 (HH36, D10) chicken embryonic hearts for dynamic imaging of ventricular development.

Heart slices were prepared using vibratome sectioning and evaluated for physiological and cellular viability during ex vivo culture. A 5.5% agarose concentration was identified as optimal for producing stable 200-µm heart slices. Tissue viability was assessed through spontaneous beating frequency and immunohistochemical analysis of proliferation and apoptosis. Beating frequency increased significantly between 1 and 2 hours, demonstrating that the tissue required an initial recovery period following mechanical stress from isolation and vibratome sectioning followed by a consistent beating throughout 8 hours post slicing.

Expanded immunohistochemical analysis demonstrated significantly lower $pHH3^{+}/DAPI^{+}$ proliferation in cultured slices compared with in vivo hearts, while $Caspase\text{-}3^{+}/DAPI^{+}$ apoptosis did not significantly differ across culture conditions. These results establish a viable platform for live imaging while identifying cellular changes associated with ex vivo culture.

Summary of Research:

The embryonic ventricular wall consists of compact myocardium, a dense outer layer, and trabecular myocardium, an inner network of muscular projections.

Coordinated development and remodelling of these regions are necessary for normal ventricular formation. Conventional histology provides static images of cardiac structure but cannot capture the dynamic cellular movements responsible for tissue remodelling. Therefore, this project aimed to establish a live embryonic heart-slice culture system that could preserve tissue function while enabling confocal time lapse imaging of ventricular morphogenesis.

Chicken embryos were incubated to HH36 (D10) and embryonic hearts were isolated, embedded in agarose, and sectioned into approximately 200-µm slices using a vibratome. Agarose concentration was optimized to provide sufficient structural support while allowing successful sectioning. A 6% concentration was too rigid, whereas 5% did not provide adequate support; 5.5% produced stable slices suitable for imaging. Confocal microscopy was then used for live imaging, while fixed slices were analysed using immunohistochemistry. MF20 was used to identify cardiomyocytes, DAPI to identify nuclei, phosphorylated histone H3 (pHH3) to identify proliferating cells, and Caspase-3 to identify apoptotic cells. Positive cells were quantified using ImageJ, and marker positive cells were normalized to total nuclei to generate $pHH3^{+}/DAPI^{+}$ and $Caspase\text{-}3^{+}/DAPI^{+}$ ratios.

Physiological viability was initially assessed by measuring spontaneous beating at 0, 1, 2, 4, 6, and 8 hours after sectioning. Beating frequency was significantly lower at 1 hour than at 2 hours after sectioning (paired t-test, $t(16) = -5.27$, $p = 7.63 \times 10^{-5}$), indicating that the tissue required an initial recovery period following mechanical stress from isolation and vibratome sectioning.. Following recovery, beating remained stable from 2–8 hours (repeated-measures ANOVA, $F(3,48) = 0.601$, $p = 0.617$). However, no significant difference in beating frequency was observed from 2–8 hours, indicating that cardiac function remained stable following recovery. This supported approximately 2 hours as an appropriate recovery period before long-term live imaging.

The expanded immunohistochemical analysis provided additional information about cellular activity. $pHH3^{+}/$

DAPI$^+$ ratios decreased from 0.0351 in vivo to 0.0187, 0.0169, 0.0141, and 0.00925 at 2, 4, 6, and 8 hours, respectively. A one-way ANOVA demonstrated a significant difference among groups ($F(4,48) = 4.110$, $p = 0.00606$). Compared with in vivo hearts, proliferation was significantly lower at 2 hours ($p = 0.0231$), 4 hours ($p = 0.0100$), 6 hours ($p = 0.00353$), and 8 hours ($p = 0.000821$). Thus, although the slices remained contractile, their proliferative activity was reduced compared with normal in vivo tissue.

In contrast, Caspase-3 analysis did not demonstrate a significant overall difference among groups ($F(4,53) = 2.071$, $p = 0.0976$). Comparisons with in vivo hearts were also not significant at 2 hours ($p = 0.132$), 4 hours ($p = 0.918$), or 6 hours ($p = 0.108$). These findings suggest that ex vivo culture did not produce a statistically detectable increase in apoptosis within the available dataset.

Regional analysis also showed no significant overall difference between compact and trabecular myocardium for either marker. For pHH3, the combined compact mean was 0.0183 compared with 0.0116 in trabecular myocardium ($p = 0.0712$). For Caspase-3, the combined means were 0.0238 and 0.0233, respectively ($p = 0.907$). Therefore, regional differences in proliferation or apoptosis alone do not appear sufficient to explain ventricular remodelling at this developmental stage.

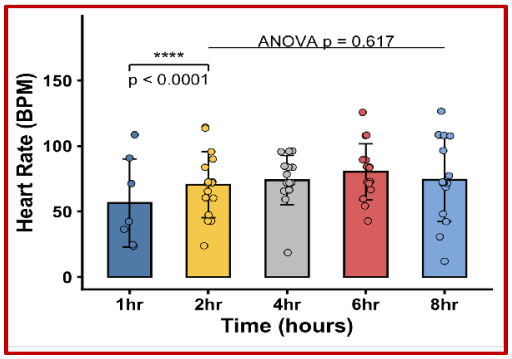

Figure 1: Heart rate (BPM) over a time period of 8 hours. Heart rate increased significantly from 1 hr to 2 hr ($p < 0.0001$) then remained stable from 2–8 hr (ANOVA, $p = 0.617$).

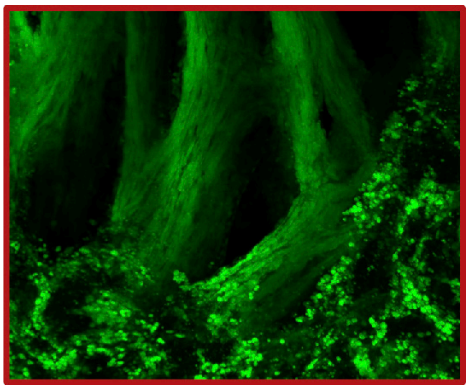

Figure 2: Immunohistochemical stained picture of compact and trabacular region of a H.H stage 34 embryonic heart ventricle.

Conclusions and Future Steps:

The optimized D10 heart-slice culture platform successfully maintained spontaneous cardiac activity for at least 8 hours following an approximately 2-hour recovery period. This supports its use for long-term live confocal imaging and dynamic investigation of ventricular morphogenesis. However, the immunohistochemical results demonstrate that while beating remained stable and apoptosis did not significantly increase, proliferation was significantly lower in cultured slices than in normal in vivo hearts which can be an indication of active remodelling sacrificing the rate of proliferation.

The lack of significant regional differences in proliferation and apoptosis between compact and trabecular myocardium suggests that ventricular wall remodelling may involve mechanisms beyond regional changes in cell division or cell death. Dynamic cellular movement, tissue deformation, and trabecular compaction may contribute substantially to ventricular morphogenesis and can be investigated using the established live imaging platform.

Future work will focus on HH38/D12 heart slices analyses to determine whether tissue viability and cellular remodelling at later developmental stages. Comparing D7, D10 and D12 hearts will allow developmental changes in ventricular morphogenesis to be characterized. Further analysis of compact versus trabecular regions will help determine their respective contributions to ventricular wall remodelling. Ultimately, this platform can be applied to congenital heart disease models, including Hypoplastic Left Heart Syndrome (HLHS), to investigate how abnormal cellular morphogenesis contributes to defective ventricular development.

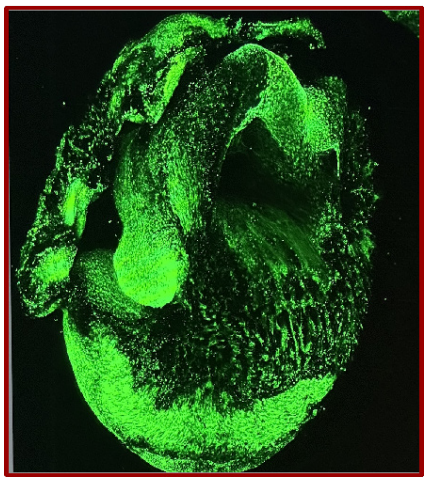

Figure 3: Overview of immunohistochemically stained image of H.H stage 34 embryonic heart.

Pediatric Heart-Assist System for Congenital Heart Failure in Infants & Children: Silicone Coating and Delivery-System Development

CNF Intern: Renata Ortega
Student Affiliation: Miguel A. Loya College of Engineering, Engineering Innovation & Leadership in Biomedical Engineering, The University of Texas at El Paso

Summer Program(s): 2026 Cornell Cardiac Undergraduate Research Experience (CURE)
Mentor(s): James Antaki, Biomedical Engineering, Cornell University; Rugveda Thanneeru, Antaki Laboratory
Primary Source(s) of Research Funding: American Heart Association
Contact: rorteganun@miners.utep.edu, antaki@cornell.edu, rt473@cornell.edu
Summer Program Website(s): https://www.cnf.cornell.edu/education/reu

Abstract:

The ventricular connection is a critical component of an implantable pediatric heart-assist system. This project investigated silicone coating and delivery of a braided Nitinol cannula intended for sutureless left ventricular access. Work included material screening, dip-coating trials, preparation of MED-2014/xylene formulations, and development of an alternative release mechanism. An acute ovine study achieved transapical access, hemostasis, and initial cannula advancement, but incomplete flange deployment revealed limitations of the tear-strip delivery system. A helmet-style tip was subsequently developed, and ex vivo testing demonstrated flange opening while identifying friction-induced premature release. These findings linked coating quality to insertion and deployment behavior and established priorities for the next prototype: reproducible coating, controlled retention, and reliable flange release.

Summary of Research:

PediaFlow is a miniature, magnetically levitated ventricular assist device developed for infants and young children. Its development has combined computational design with experimental evaluation of hydraulic performance and blood compatibility [1,2]. The ventricular connection must also accommodate small anatomy and maintain unobstructed inflow. Prior work by Antaki and colleagues showed that cannula geometry and positioning affect intraventricular flow and susceptibility to obstruction [3].

Cannula Architecture and Fabrication

The cannula consists of a braided, shape-set superelastic Nitinol frame, a silicone membrane, and a deployable distal flange (Figure 1). The frame provides a collapsible structure, while the coating is intended to form a flexible, blood-tight conduit. The distal flange is designed to conform to the endocardial surface and provide sutureless anchoring [3]. Fabrication and delivery must preserve both membrane integrity and flange expansion following release from the compressed configuration.

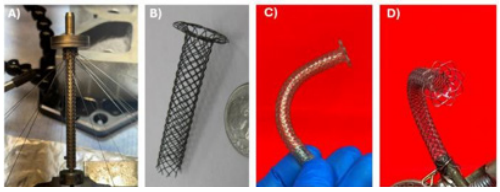

Figure 1: Ventricular cannula fabrication: (A) Nitinol braiding, (B) shape-set frame, (C) silicone dip-coated cannula, and (D) deployed distal flange.

Silicone Material Screening

Material evaluation considered silicone viscosity, tear resistance, elongation, processing time, and intended implant duration. The process comparison included MED10-6400, MED6-6606 RTV silicone, and MED-2014. Additional screening covered MED-6600, MED-6615, MED-2214, and Elast-Eon E2As. MED-2014 became the working formulation for the dip-coating trials. It is a fully compounded silicone dispersion in xylene suitable for heat-cured thin films; the manufacturer excludes human implantation beyond 29 days, so its selection addressed prototype and acute-study needs [4].

Dip-Coating Formulation and Thermal Processing

The initial coating bath contained 40 mL of MED-2014 dispersion and 5 mL of added xylene. Subsequent coats used 30 mL of dispersion and 8 mL of xylene. Both formulations were vacuum-deaired until visible bubbles were eliminated. Increased dilution in subsequent coats was intended to limit film buildup while maintaining coverage of the braided frame. These ratios describe the supplied dispersion and added solvent

The processing schedule recorded for MED-2014 comprised 1h at 50°C, 1h at 150°C, and at least 3 h of ambient stabilization, consistent with the manufacturer's property-conditioning schedule [4]. Consultation with

NuSil addressed bubble removal, mandrel release, withdrawal control, and convection-oven airflow. Shorter drying intervals and MED10-6640, a higher-tear-strength candidate, were identified for further evaluation. Residual-solvent and mechanical testing remain necessary before adopting a shortened process.

Acute In Vivo Evaluation in an Ovine Model

An acute ovine study assessed transapical penetration, hemostasis, cannula advancement, and distal flange deployment in collaboration with the Cornell College of Veterinary Medicine team (Figure 2). Ventricular access and initial advancement were achieved with hemostasis maintained. Tear-strip fracture prevented complete intraventricular flange deployment. Insertion depth and position were difficult to resolve, and echocardiographic assessment did not provide sufficient wall-thickness information for reliable placement. The principal failure mode was incomplete mechanical release, motivating revision of the delivery mechanism and improved control of insertion depth.

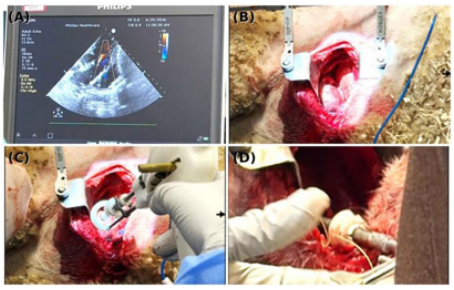

Figure 2: Acute ovine evaluation: (A) echocardiographic assessment, (B) LV apical exposure, (C) positioning of the delivery system, and (D) trigger-actuated deployment attempt. Distal flange deployment remained incomplete.

Delivery Mechanism Redesign

Alternative concepts included tubing-based confinement, telescopic components, and axial pusher mechanisms. The helmet-tip design used a distal cap to retain the compressed cannula during insertion. Relative axial displacement of the tip and cannula releases the flange for expansion (Figure 3). Design objectives were to eliminate the external tear-strip material, minimize the insertion profile, and separate tissue penetration from controlled flange release.

An ex vivo heart connected to a mock circulatory loop supported assessment of cannula placement and alternative delivery (Figure 4). Cap/helmet testing demonstrated flange expansion, although nonuniform silicone coating was associated with increased insertion friction. In one attempt, proximal displacement of the cannula relative to the tip caused premature release. This observation identified an interaction between coating uniformity, axial retention, and deployment timing. Reduced flange-coating thickness and a mechanical retention feature were proposed to limit unintended displacement during insertion.

Figure 3: Delivery-system development, left to right: current prototype, helmet-tip CAD concept, and sleeveless delivery tip.

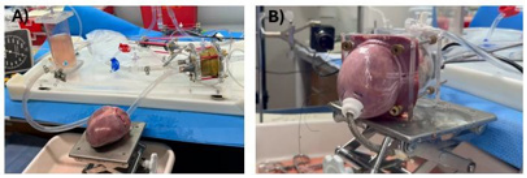

Figure 4: Ex vivo evaluation: (A) mock circulatory loop and (B) ventricular apex cannulation with an alternative delivery system.

Conclusions and Future Steps:

This work established a working MED-2014 dilution approach and identified how coating uniformity affects cannula delivery. Acute testing demonstrated ventricular access and hemostasis, while flange release remained the principal procedural limitation. The helmet-tip concept enabled ex vivo deployment. Next steps are to standardize coating thickness, evaluate a single flange-coating layer, measure insertion and retention forces, and repeat deployment testing with defined success criteria. Solvent removal and coating durability should be verified before further animal studies; long-term support will require an appropriately qualified material.

Acknowledgements:

This work was performed in the Antaki Laboratory at Cornell University. Thanks to Dr. James Antaki, Dr. Rugveda Thanneeru, the Cornell College of Veterinary Medicine team, and the CNF/CURE REU program staff for mentorship and experimental support.

References:

[1] Antaki JF, et al. PediaFlow Maglev Ventricular Assist Device: A Prescriptive Design Approach. Cardiovasc Eng Technol. 2010;1:104-121. doi:10.1007/s13239-010-0011-9.

[2] Olia SE, et al. Preclinical performance of a pediatric mechanical circulatory support device: The PediaFlow ventricular assist device. J Thorac Cardiovasc Surg. 2018;156:1643-1651.e7. doi:10.1016/j.jtcvs.2018.04.062.

[3] Bachman TN, Bhama JK, Verkaik J, Vandenberghe S, Kormos RL, Antaki JF. In-vitro Evaluation of Ventricular Cannulation for Rotodynamic Cardiac Assist Devices. Cardiovasc Eng Technol. 2011;2:203-211. doi:10.1007/s13239-011-0050-x.

[4] NuSil Technology. MED-2014: Silicone dispersion. Technical data sheet, Rev. C, November 16, 2018.

Thermomechanical Nanomolding of Single Crystalline CoSn Nanowires

CNF Summer Student: Bruce Pan
Student Affiliation: College of Chemistry, University of California, Berkeley

Summer Program(s): 2026 Cornell NanoScale Facility Research Experience for Undergraduates (CNF REU) Program

Principal Investigator(s): Judy J. Cha, Cornell University

Mentor(s): Jack Coyle

Primary Source(s) of Research Funding: NSF SUPREME REU

Contact: judy.cha@cornell.edu, bdp@berkeley.edu, jdc384@cornell.edu

Summer Program Website(s): https://www.cnf.cornell.edu/education/reu

Research Group Website: cha.mse.cornell.edu

Primary CNF Tools Used: Nabity NPGS Nanometer Pattern Generator System; Carl Zeiss GeminiSEM 560 scanning electron microscope

Abstract:

Copper interconnect resistivity climbs as line dimensions shrink because electrons scatter at surfaces and grain boundaries. CoSn is a kagome metal that carries current more easily along the c direction than in the basal plane, which makes c direction CoSn nanowires worth evaluating as a replacement conductor. This project used thermomechanical nanomolding to press bulk CoSn into nanoporous anodic aluminum oxide and release wires in dilute hydrofluoric acid. Scanning transmission electron microscopy found many single crystal wires with [001] long axes, and energy dispersive X ray spectroscopy returned normalized fractions of 50.64 atomic percent cobalt and 49.36 atomic percent tin. Four terminal devices were built on single wires, but rectifying contacts prevented extraction of an intrinsic resistivity.

Summary of Research:

Cobalt atoms in CoSn sit on kagome nets stacked along the c axis, which produces flat bands near the Fermi level [4]. Single crystal measurements put the basal plane resistivity more than an order of magnitude above the c axis value [5], and films reach about 13 microohm centimeters along c [6]. Neither geometry shows how resistivity behaves once the conductor is confined to a nanoscale cross section [7]. The aim was to mold c direction single crystal nanowires and measure them individually.

Feedstock was pressed against a nanoporous anodic aluminum oxide template at 550 degrees Celsius and 250 megapascals for two hours, so metal fills the pores by pressure driven diffusion rather than melting [1,2,3]. The template was dissolved in 5 weight percent hydrofluoric acid and the wires sonicated and drop cast onto marked substrates. Of five molding runs, CS4 yielded nothing, which we attribute to insufficient effective pressure.

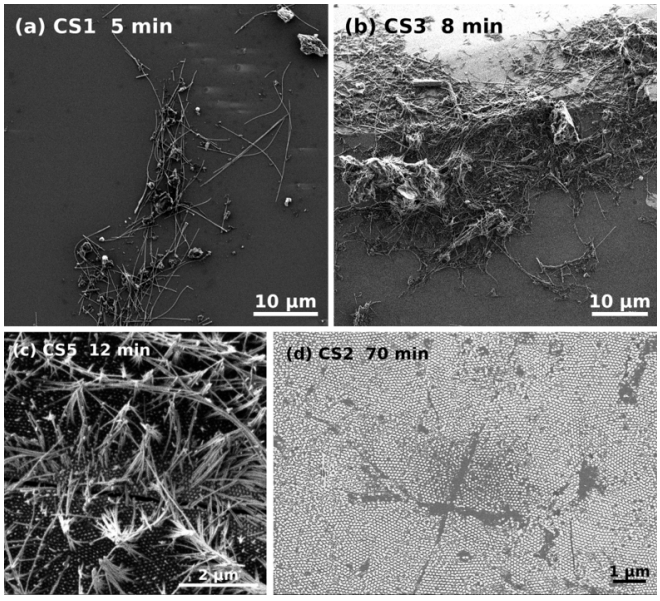

Figure 1: Released material after 5, 8, 12 and 70 minutes in 5 weight percent hydrofluoric acid. Twelve minutes gave the cleanest dense arrays in this sample set.

Release time controls how much product survives, and Figure 1 brackets it. Five minutes left sparse fragments in undissolved template. Eight minutes freed more material but left it matted in residue. Twelve minutes gave the cleanest dense arrays. Seventy minutes removed the wires and left only stubs. Filling fraction, delamination and handling also varied between runs, so this is a usable window rather than a universal optimum.

Scanning electron microscopy showed structures several micrometers long at the 40 nanometer nominal diameter set by the template. One frame gave an apparent width of 52.19 nanometers, which we did not treat as physical because aperture and stigmation were not optimized. Collaborator imaging at the Cornell Center for Materials Research resolved the lattice directly. Figure 2 shows wires along [120] and [110], both single crystalline with [001] long axes, so many wires grow with the fast axis

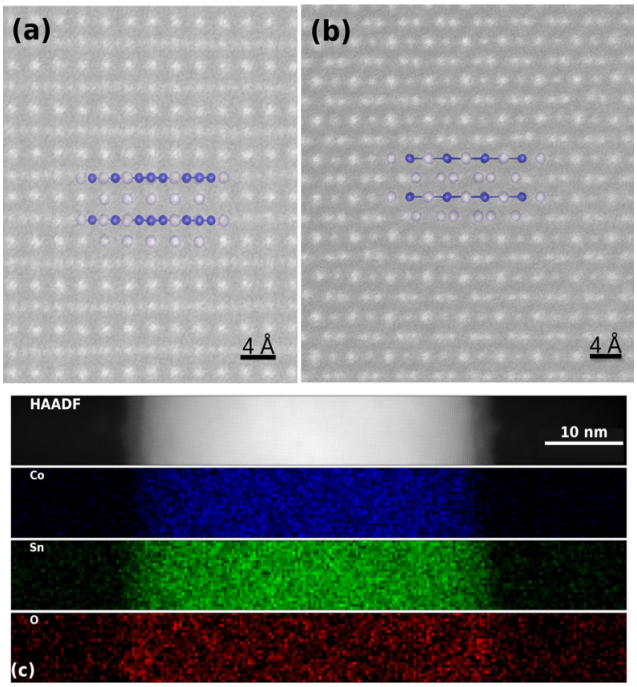

Figure 2: Atomic resolution high angle annular dark field imaging of single crystal CoSn nanowires along [120] in (a) and [110] in (b), both with [001] long axes, with elemental maps across a wire cross section in (c) showing cobalt and tin in the core and oxygen at the surface.

along the wire. Elemental maps confirm cobalt and tin throughout the core. Quantification normalized to those two elements gave 50.64 and 49.36 atomic percent, each with 3.17 percent reported error, consistent with 1:1 stoichiometry. Oxygen at the surface suggests a thin tin oxide shell of undetermined thickness.

Four electrodes were patterned across a single wire by electron beam lithography on the Nabity Nanometer Pattern Generator System at the Cornell NanoScale Facility, with contact metal deposited at the Cornell Center for Materials Research. Inner probe spacing was 2.49 micrometers. Figure 3 shows a completed device and the most common failure mode, where the wire dislodges during processing and the electrodes land on bare substrate. Yield was limited more by wire retention than by lithography.

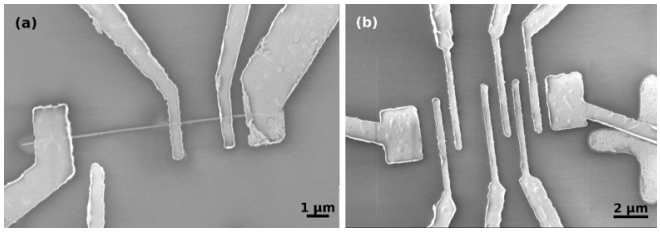

Figure 3: Four terminal device on a single CoSn nanowire in (a), and in (b) a set of electrodes left with no wire after the wire was dislodged during processing.

Electrical testing used a Keysight B1500A parameter analyzer. Two point sweeps between contact pairs are collected in Figure 4. Most pairs were close to linear over plus or minus 100 nanoamperes, which initially suggested usable contacts, but one pair rectified strongly and is plotted against the right hand axis. Alternating current measurement then identified one contact as Schottky and returned roughly 12 megohms of apparent four terminal impedance. Because drive frequency, amplitude and phase were not retained, that number cannot be assigned as a resistance. Other devices were also nonohmic, so no intrinsic resistivity or contact resistance was extracted.

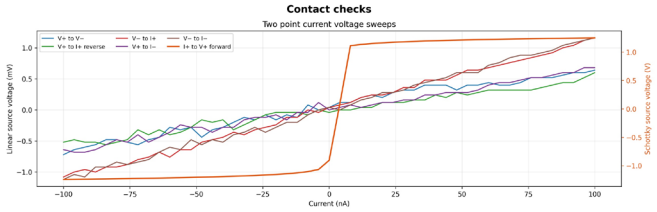

Figure 4: Two point current voltage sweeps between contact pairs. The rectifying pair uses the right hand axis. Alternating current measurement later identified one Schottky contact on this device.

Conclusions and Future Steps:

Nanomolding produced long CoSn nanowires, microscopy confirmed many single crystal wires with [001] long axes and the expected composition, and four terminal device fabrication was demonstrated. The contacts, not the supply of wires, stopped the transport measurement. Next steps are to treat the wire surface before metal deposition, improve wire adhesion during processing, check every contact pair for ohmic behavior before a four terminal sweep, and keep the full alternating current settings and raw data. Resistivity can then be measured across several diameters to test scaling directly.

References:

[1] Z. Liu et al., "Nanomolding of Crystalline Metals: The Smaller the Easier," Physical Review Letters 122, 036101 (2019).

[2] N. Liu et al., "General Nanomolding of Ordered Phases," Physical Review Letters 124, 036102 (2020).

[3] M. T. Kiani and J. J. Cha, "Nanomolding of Topological Nanowires," APL Materials 10, 080904 (2022).

[4] M. Kang et al., "Topological Flat Bands in Frustrated Kagome Lattice CoSn," Nature Communications 11, 4004 (2020).

[5] H. Huang et al., "Flat-Band-Induced Anomalous Anisotropic Charge Transport and Orbital Magnetism in Kagome Metal CoSn," Physical Review Letters 128, 096601 (2022).

[6] T. Nakatani et al., "Fabrication and Characterization of Single-Crystalline CoSn (10−10) Kagome Metal Thin Films for Interconnect Applications: Structure and Anisotropic Electrical Resistivity," Applied Physics Letters 127, 203302 (2025).

[7] M. T. Kiani and J. J. Cha, "Shrinking Interconnects beyond Copper," Science 390, 572 to 573 (2025).

Qualifying the ASML Job Scriptor for CNF Use

CNF Intern: Shantanu Patel
Student Affiliation: Materials Science and Engineering, Cornell Univeristy

Summer Program(s): 2026 Cornell NanoScale Facility Summer Internship

Mentor(s): John Treichler, CNF

Primary Source(s) of Research Funding: NORDTECH

Contact: sp2676@cornell.edu, treichler@cnf.cornell.edu

Summer Program Website(s): https://www.cnf.cornell.edu/education/reu

Primary CNF Tools Used: ASML PAS 5500 Stepper, Heidelberg DWL2000 Mask Writer, Optical Microscope

Abstract:

The ASML deep ultraviolet (DUV) Stepper, while precise and controlled for semiconductor manufacturing, is susceptible to human error in Micro-Electro-Mechanical Systems and optical device fabrication, which require complex exposure patterns and specialized alignment. For this reason, the goal was to qualify a new tool update: the Job Scriptor. This process began by testing and validating multiple computer-aided design (CAD) layouts. The project simulated a job with the ASML Stepper and fabricated a photomask for experimental comparison. The resulting software simplifies the generation of complex job files for the ASML lithography stepper by enabling off-site job creation, allowing users to prepare their work before entering the cleanroom. In conclusion, this update will let users perform more complex photolithography processes, paving the way for advanced automation in optical-device fabrication.

Summary of Research:

The goal of this project was to qualify the ASML Stepper's new feature update, the Job Scriptor, for CNF use. This Job Scriptor simplifies photolithography processes in the cleanroom, unlike the conventional workflow where users must manually input parameters into the tool. It allows users to visualize the complete exposure plan beforehand with specific parameters like reticle positioning and exposure fields. As a result, users can ensure correct placement of every pattern before the job is executed, reducing the risk of costly fabrication errors.

The qualification process started with creating a CAD layout of a wafer-scale exposure pattern to compare with its experimental and computational simulations. The CAD layout represented a wafer-scale pattern containing an array of repeated test structures with pattern leads that electrically connect to contact pads for potential transport measurements. Creating this layout required using the GDSTK library in Python to generate 1,000,000 squares, each 1 micron in length, along with a set of leads in the center of the design. This layout was meant to test the Job Scriptor's ability to produce repeated test structures while retaining the design's central geometry. After creating the CAD layout, the project moved to photomask fabrication in the cleanroom. This involved using the DWL2000 Heidelberg Mask Writer, which used a high-resolution, high-speed laser to pattern a photosensitive chromium-coated mask plate. The fabricated photomask would be used as an experimental comparison with our CAD layout.

After fabrication, the ASML Stepper's Job Scriptor used the CAD file to verify its functionality. This helped simulate the intended exposure layout to examine the Job Scriptor's performance. The Stepper accurately reproduced the CAD layout into an exposure job, producing a large 1,000 x 1,000 array inside a circle, filled with 1,000,000 repeated 1 μm structure squares. Validating this software involved four main criteria: central exposure region present, exposure region centered, wafer orientation preserved, and no unintended features. Each qualification criterion was met, demonstrating that the Job Scriptor successfully translated a CAD layout into a simulated exposure image.

Before fully qualifying the ASML Stepper Job Scriptor, optical microscopy examined the quality of leads on the fabricated mask. Experimental comparison included three main features: a central exposure region present, an exposure region centered, and wafer orientation preserved with the CAD layout. These leads were placed on the photomask to fabricate contact pads for potential material characterization. They were then examined under an optical microscope and used to qualify the ASML Stepper Job Scriptor. Because the microscopy showed that the fabricated structures matched the intended CAD geometry based on these three features, the Job Scriptor was successfully qualified for CNF use.

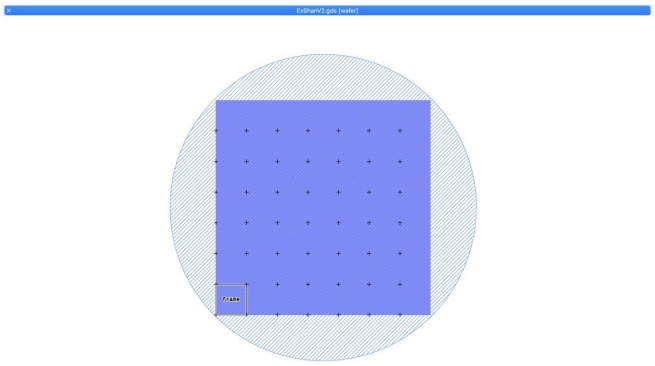

Figure 1: CAD layout showing a wafer with repeated structures and leads inside.cleaned with IPA.

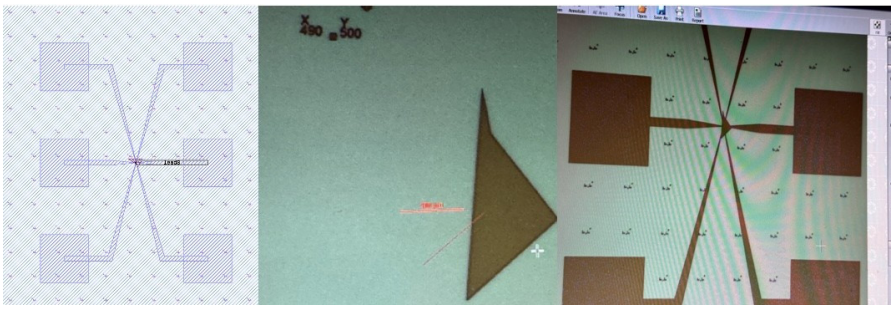

Figure 2: Comparison of CAD layout with experimental results under an optical microscope.

Validation criterion	CAD Design	Generated Result	Outcome
Central exposure region present	Yes	Yes	Pass
Exposure region centered	Yes	Yes	Pass
Wafer orientation preserved	Yes	Yes	Pass
No unintended features	None	None	Pass

Figure 3: Qualification criteria comparing the CAD layout with the generated ASML job.

Figure 4:Workflow used to qualify the ASML Stepper Job Scriptor for CNF use.

Conclusions and Future Steps:

This project qualified the ASML Stepper's new Job Scriptor update for future CNF use, both using experimental and software-based validation. This will greatly simplify job generation for CNF users by enabling offsite job creation and future capabilities in lithography workflows, such as multi-image stepping distances. It will allow users to visualize the complete wafer patterning before exposure, as well as specific parameters like die placement and reticle positioning. Overall, this update will not only reduce fabrication errors but also significantly lower the costs associated with them. This will increase throughput and improve user experience with photolithography.

Qualifying the ASML Stepper's Job Scriptor for CNF use will also enable a wide range of future lithography applications. For example, it will enable users to prepare jobs containing multiple device designs/exposure fields, potentially paving the way for devices like Micro-Electro-Mechanical Systems that require unusual geometry, driving advances in the field of electronics. This new software can also be integrated into the CNF design workflow by enabling new capabilities such as graphical user interface (GUI)-based interactive wafer visualization and focus/exposure matrices.

References:

[1] Bordonaro, G., & Treichler, J. (2020, January). Heidelberg DWL 2000 Laser Writer. https://www.cnfusers.cornell.edu/sites/default/files/Equipment-Resources/DWL2000Manual2020.pdf.

[2]. Cornell Nanoscale Science and Technology Facility. (2020). ASML job cheat sheet. https://www.cnfusers.cornell.edu/sites/default/files/Equipment-Resources/ASML%20Job%20Cheat%20Sheet2020.pdf.

Characterization of Deep Reactive Ion Etching for Silicon Plasma Singulation

CNF Intern: Caleb Pelland
Student Affiliation: Department of Materials Science and Engineering, Cornell University

Summer Program(s): 2026 Cornell NanoScale Facility Summer Internship
Mentor(s): Jeremy Clark, CNF
Primary Source(s) of Research Funding: NORDTECH
Contact: cap363@cornell.edu, clark@cnf.cornell.edu
Summer Program Website(s): https://www.cnf.cornell.edu/education/reu

Abstract:

Bosch deep reactive ion etching (DRIE) was characterized for silicon plasma singulation using SPR 220-4.5 positive photoresist [1]. A 250 cycle study quantified aspect-ratio-dependent etching (ARDE) from 5–100 µm dicing streets, or trenches. Long runs established local 30 µm through-wafer capability and the photoresist limit. Depth decreased from 460.59 µm at 100 µm width to 222.64 µm at 5 µm. A cycle-dependent passivation run showed 0.80–1.00 µm widening, compared with provisional fixed-passivation values of 4–7 µm at matched widths. Optical monitoring identified mask failure but did not qualify a silicon endpoint.

Summary of Research:

1. Campaign from Screening to Final Monitor

Each Bosch cycle [2] used 2.2 s of C4F8-rich polymer passivation, a 2.0 s ion-assisted SF6 trench-bottom clear at 275 W platen bias, a 3.0 s zero-bias high-flow SF6 silicon etch, and a 1.0 s low-flow SF6 transition. Fixed passivation means that the 2.2 s step did not change with cycle number. Reflectometry measured resist loss, and scanning electron microscopy (SEM) measured depth. Aspect ratio was depth divided by nominal width, D/w. Normalized depth was $Dw/D100$.

2. Selectivity and Photoresist Survival

A five-run platen-bias/passivation-time screen was completed. Both streaked 225 W conditions were rejected. Accepted conditions spanned 53.45–57.37 nm/cycle and 6.38:1–10.03:1 silicon-depth/resist-loss selectivity. The non-flat 29.27:1 result was rejected for anomalously small resist loss. Clearing trials selected the 275 W/2.2 s fixed-passivation process.

The 350 cycle photoresist-survival run reduced center resist from 3789.592 nm to 542.434 nm, corresponding to 9.278 nm/cycle consumption. Site loss was 2.896–3.247 µm. With nominal 530 µm silicon, the conditional thickness-to-loss ratio was 163:1–183:1. It represents selectivity only where clearing is independently confirmed, not full-wafer mask uniformity. 500 cycle testing cleared 30 µm streets but consumed the photoresist, motivating a more durable oxide or metal hard mask for narrower features [3].

Dense repeated streets with 33.8% open area lost resist, while normally spaced 30 µm die streets with 2.7% open area retained it. This is not a universal density threshold. Silicon depth was not mapped, so accelerated local silicon etching is unproven.

3. Photoresist Loss Decreased with Radius

Matched thin-film reflectometry measurements show radial photoresist consumption. Photoresist-survival sites decreased from 9.23 nm/cycle in the inner radial bin to 8.37 nm/cycle near the edge. The ramped-passivation run decreased from 9.03 nm/cycle to 7.57 nm/cycle. Linear slopes were −0.029 and −0.046 nm/cycle/mm. These are resist-loss, not silicon etch-rate, measurements.

4. ARDE is the Dominant Small-Street Limit

The 250-cycle measurements in Table 1 decrease monotonically with narrower streets. Image scaling was calibrated, but mounting and projection uncertainty were not quantified. The 5 µm trench had a 44.53:1 nominal-width ratio but only 48.3% of the 100 µm-street depth. Through 530 µm silicon would require a geometric ratio near 106:1.

Width (µm)	Depth (µm)	D/w	D_w/D_{100}
5	222.64	44.53	0.483
15	256.04	17.07	0.556
30	306.13	10.20	0.665
50	395.19	7.90	0.858
100	460.59	4.61	1.000

Table 1: SEM-measured depth, nominal-width aspect ratio, and depth normalized to the 100 µm street after 250 fixed-passivation cycles. Each width has one cross-section.

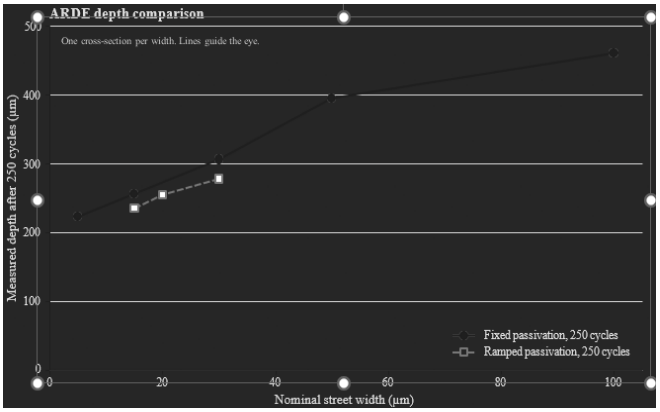

Figure 1: SEM-measured silicon trench depth after 250 Bosch cycles versus nominal opening width. A fixed 2.2 s polymer-passivation step is compared with a linear increase from 2.2–2.5 s. Each point is one cross-section. Lines guide the eye.

5. The Ramped-Passivation Run Showed Less Widening

The ramped-passivation run increased the polymer-deposition step from 2.2 s to 2.5 s over 250 cycles, as a depth-compensation strategy [4], [5]. Confirmed 15, 20, and 30 µm trenches reached 234.95, 254.87, and 277.86 µm, with 0.801, 0.591, and 1.000 µm top-to-bottom widening. Relative to the fixed-passivation depth study's provisional 15 µm and 30 µm widening of 4 and 7 µm, the new values were 80% and 86% smaller. Depth was 8.2% and 9.2% lower at those widths. Nominal-width aspect ratios were 15.66:1, 12.74:1, and 9.26:1. Each profile has one cross-section and no replicate uncertainty.

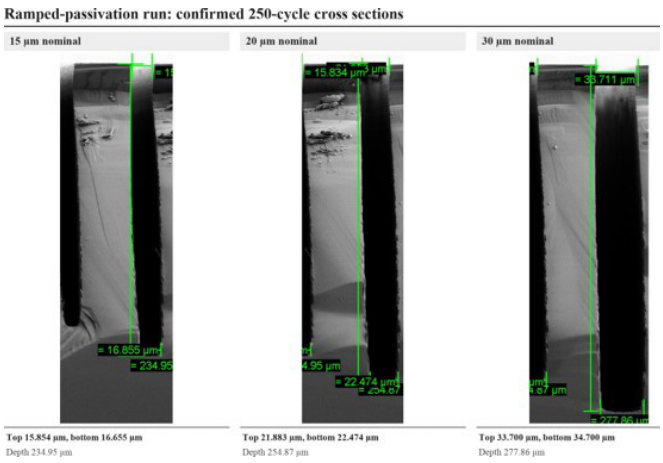

Figure 2: Cross-sectional SEMs after the 250-cycle ramped-passivation process show top width, bottom width, and depth for nominal 15, 20, and 30 µm streets. Green annotations are instrument measurements. No geometric correction was applied.

6. Optical Monitoring Detected Mask Failure, Not Silicon Breakthrough

Optical emission spectroscopy (OES) monitoring was evaluated as a possible method for stopping the etch when silicon streets clear [6], [7]. The trial established a compact data-collection method and identified a late optical transition associated with local photoresist loss. It did not establish a silicon-breakthrough endpoint because the transition was not correlated with physical clearing of 30 µm streets. Automatic termination therefore remains outside the characterized process scope until the optical transition is reproduced and verified against physical breakthrough.

Conclusions and Future Steps:

Fixed passivation enabled normally spaced 30 µm streets with bottom widening. Ramped passivation showed less widening but lower depth. ARDE, pattern density, and mask survival constrain smaller streets. Hard masks are the smaller-street path. Optical termination remains disabled pending repeatable physical clearing.

Acknowledgements:

This work was performed at the Cornell NanoScale Facility (CNF), part of the National Nanotechnology Coordinated Infrastructure supported by National Science Foundation Grant NNCI-2025233. Jeremy Clark and CNF staff are acknowledged. This internship was sponsored by NORDTECH.

References:

[1] Kayaku Advanced Materials, MEGAPOSIT SPR220 Series Photoresists product data sheet, Kayaku Advanced Materials. [Online]. Available: https://kayakuam.com/wp-content/uploads/2019/09/SPR220-Data-Sheet. pdf.

[2] F. Laermer and A. Schilp, "Method of anisotropically etching silicon," US 5,501,893, Mar. 26, 1996. [Online]. Available: https://patents.google.com/patent/ US5501893A/en.

[3] M. S. Gerlt, N. F. Läubli, M. Manser, B. J. Nelson, and J. Dual, "Reduced etch lag and high aspect ratios by deep reactive ion etching (DRIE)," Micromachines, vol. 12, no. 5, p. 542, 2021. doi: 10.3390/mi12050542.

[4] B. Chang, P. Leussink, F. Jensen, J. Hübner, and H. Jansen, "DREM: Infinite etch selectivity and optimized scallop size distribution with conventional photoresists in an adapted multiplexed bosch DRIE process," Microelectronic Engineering, vol. 191, pp. 77–83, 2018. doi: 10.1016/j.mee.2018.01.034.

[5] Y. Tang, A. Sandoughsaz, K. J. Owen, and K. Najafi, "Ultra deep reactive ion etching of high aspect-ratio and thick silicon using a ramped-parameter process," Journal of Microelectromechanical Systems, vol. 27, no. 4, pp. 686–697, 2018. doi: 10.1109/JMEMS.2018.2843722.

[6] Plasma-Therm LLC, Cortex mds documentation, Offline Help supplied with the MDS system; copyright 2013–2015, Plasma-Therm LLC, 2015.

[7] Plasma-Therm LLC, Endpointworks 4 user's guide and integrated help, Offline Help supplied with EndpointWorks 4, Plasma-Therm LLC, 2022.

ST-FMR measurements of low-symmetry van der Waals material $TaIrTe_4$

CNF Summer Student: Danaan Perry
Student Affiliation: Department of Physics, University of Illinois at Urbana-Champaign

Summer Program(s): 2026 Cornell NanoScale Facility Research Experience for Undergraduates (CNF REU) Program
Principal Investigator(s): Daniel Ralph, Cornell University
Mentor(s): Matthew Roddy
Primary Source(s) of Research Funding: CEEMag EFRC, U.S. Dept. of Energy
Contact: dcr14@cornell.edu, danaanp2@illinois.edu, msr285@cornell.edu
Summer Program Website(s): https://www.cnf.cornell.edu/education/reu
Research Group Website: https://ralphgroup.lassp.cornell.edu/
Primary CNF Tools Used: Heidelberg MLA 150 Maskless Aligner, AJA Ion Mill, AJA Sputter Deposition, Veeco Icon AFM

Abstract:

Efficient magnetic memory requires compact storage through out-of-plane polarization as well as an energy-efficient write path. The write mechanism we are investigating uses out-of-plane spin-orbit torques (ZSOTs) to switch the magnetization of a thin ferromagnetic layer. These ZSOTs are not possible to generate in many materials due to symmetry restrictions; to overcome this, we study the low-symmetry van der Waals material $TaIrTe_4$. The current literature indicates that $TaIrTe_4$ produces strong ZSOTs, but measured values of the efficiency are inconsistent. The goal of this project is to fabricate test devices including $TaIrTe_4$ so that the efficiency of the ZSOT can be measured using the technique of spin-torque ferromagnetic resonance (ST-FMR).

Summary of Research:

Intro/Background

This project aims to contribute to the development of a write path for more energetically and spatially efficient magnetic memory. We can achieve this using the spin Hall effect. This effect occurs when running a conventional current through some spin source layer which generates a spin current that separates opposing spins on opposite surfaces of the spin source layer. This spin current can apply a torque onto the polarization of the ferromagnet, causing this magnetization to rotate. This effectively changes the state of the bit.

We are looking to examine the efficiency of TaIrTe4 as a spin source. $TaIrTe_4$ is a low-symmetry van der Waals material. This low-symmetry property gives it the potential to produce out-of-plane torques (ZSOTs) that are most efficient for switching the state out-of-plane polarized magnets needed for improved high-density memories. Current literature indicates that $TaIrTe_4$ not only produces ZSOTs, but that they are relatively strong. However, different measured values of $TaIrTe_4$'s spin Hall efficiency are inconsistent, motivating this initial exploration to validate $TaIrTe_4$'s potential as a spin source.

Fabrication

Our fabrication process begins by exfoliating flakes of $TaIrTe_4$ onto a Si/SiO_2 substrate. Bulk crystals of $TaIrTe_4$ are adhered to scotch tape and pressed onto pieces of silicon wafer. $TaIrTe_4$ is air-sensitive, so we prepared samples in a glove box to prevent air exposure before transferring to the load lock of our sputter system where exfoliation was performed. The set-up for this procedure is shown in Figure 2a. This apparatus allowed for the tape to be peeled off in vacuum as samples were loaded into the main chamber. As a van der Waals material, small, thin flakes of $TaIrTe_4$ remain stuck to the silicon, providing uniform, single crystalline thicknesses. We then deposit 4 nm of Permalloy (Py) as our ferromagnetic layer and a 2 nm Ta capping layer to prevent air exposure. We then searched for thin, even, and at a minimum 5x5 μm flakes using an optical microscope (Figure 2c). Using the Veeco Icon AFM we confirm the actual thicknesses of chosen flakes and move forward with samples that were 40 nm or less.

We then used the Heidelberg MLA 150 to perform photolithography and the AJA Ion Mill to etch our Hall bars. When milling we incorporated breaks to avoid overheating the flakes or burning the resist. We again performed lithography to pattern the contacts. Before depositing our contacts using the AJA sputter system we do a 15 minute Ar plasma clean to remove any Ta oxide and create a better connection between our Hall bar and contacts. Finally we deposit about 60 nm of Ti/Pt to create the finished device shown in Figure 1.

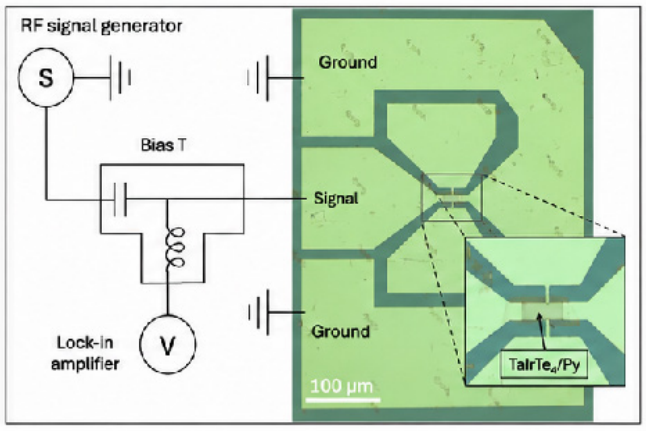

Figure 1: A completed device with GSG (ground-signal-ground) contacts for ST-FMR measurements. The enlarged area gives a closer look at the TaIrTe4/Py stack. To the left is a diagram depicting the set-up used for ST-FMR measurements.

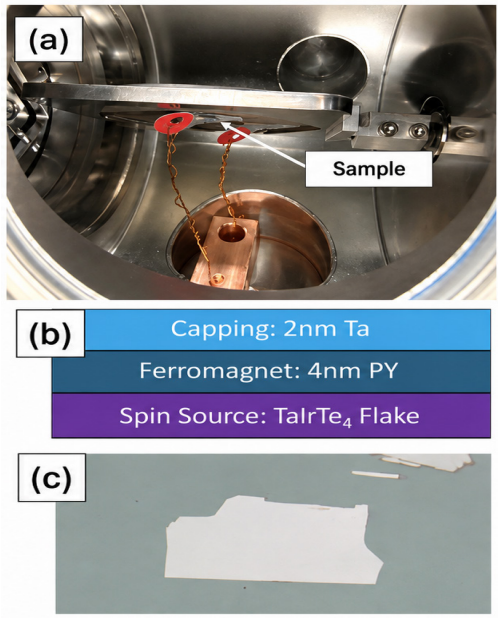

Figure 2: (a) Exfoliation apparatus in the load lock of the sputter system. (b) A complete stack consisting of a TaIrTe4 flake 20-40 nm in thickness, 4 nm Py ferromagnetic layer, and 2 nm Ta capping layer. (c) Image taken on an optical microscope of a flake with dimensions of approximately 10x20 μm.

Results

We performed spin-torque ferromagnetic resonance (ST-FMR) measurements. ST-FMR works by measuring a changing voltage (Vmix) caused by anisotropic magnetoresistance of the ferromagnetic layer. Vmix can then be graphed against the external magnetic field (Bext) and the resulting shape is a Lorentzian, pictured in Figure 4a, consisting of symmetric and antisymmetric components. These components can be separated, and their amplitudes graphed versus the angle at which the field was applied. The resulting angular dependences are shown in Figures 4b and 4c and defined by the following functions.

$$S_{total} = S^Y cos(\phi)\, sin(2\phi) + S^X sin(\phi)\, sin(2\phi) + S^Z sin(2\phi) \quad (1)$$

$$A_{total} = A^Y cos(\phi)\, sin(2\phi) + A^X sin(\phi)\, sin(2\phi) + A^Z sin(2\phi) \quad (2)$$

The ZSOTs discussed are the Z-components in the above functions, with amplitudes SZ or AZ. We are primarily concerned with the symmetric component which we see has a significant contribution from the Z-component. These results therefore indicate that $TaIrTe_4$ does produce ZSOTs, the strength of which can be determined by further analysis.

Conclusions and Future Steps:

To conclude, we fabricated functioning $TaIrTe_4$/Py devices with $TaIrTe_4$ flakes ranging from 20-40 nm thickness for ST-FMR measurements. Our initial analysis determined that $TaIrTe_4$ does produce ZSOTs and with further measurements and analysis the strength of these torques will be determined. The next steps for this include Raman spectroscopy measurements to determine the crystal axis of the samples and determine the dependence of observed ZSOTs on crystal orientation. Then taking additional measurements, such as resistivity, to obtain all variables needed to formally calculate the spin Hall conductivity of our samples.

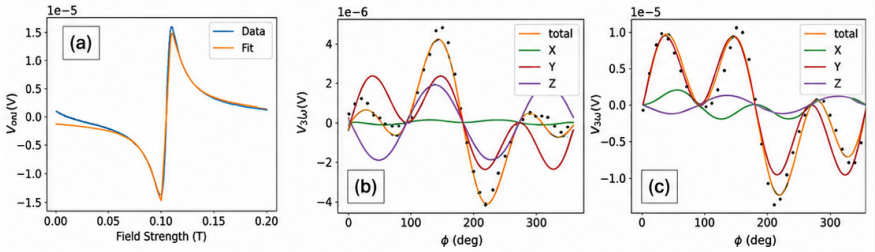

Figure 3: (a) Vmix vs. Bext results at an applied angle of 30° degrees. In blue is the raw data and in orange the Lorentzian fit. (b) and (c) display the angular dependence for the symmetric (b) and antisymmetric (c) components of Vmix. The orange line is the total fit to the raw data in blue. The green, red, and purple lines then represent the X, Y, and Z components of the total as in Equation 1.

CNF REU

Atomic Layer Deposition Dielectric Film Quality

CNF Intern: Nadiyah Rahaman
Student Affiliation: Department of Engineering, Cornell University

Summer Program(s): 2026 Cornell NanoScale Facility Summer Internship
Mentor(s): Jeremy Clark, CNF
Primary Source(s) of Research Funding: NORDTECH
Contact: nsr45@cornell.edu, clark@cnf.cornell.edu
Summer Program Website(s): https://www.cnf.cornell.edu/education/reu
Primary CNF Tools Used: Oxford FlexAL, Oxford ASP, Woolam RC-2 Ellipsometer, Kiethy Probe Station

Abstract:

As semiconductor devices continue to scale, dielectric films must become thinner while maintaining reliable electrical isolation. Atomic Layer Deposition (ALD) can be used to create thin oxide layers. These oxide layers are used to passivate electrical signals from one electrode to another with a very thin layer of oxide material. The Oxford FlexAl and Oxford ASP tools allow for thin oxide Atomic Layer Deposition (ALD) films. Deposition parameters including temperature, oxide chemistry, and ALD tool can influence film growth, density, and electrical properties. The Oxford ASP is a new ALD tool in the Cornell Nanoscale Facility (CNF) Cleanroom. The purpose of this experiment is to explore baselining the ASP. Due to tool availability and the duration of the study, the results presented represent an initial baseline rather than a complete process optimization. SiO_2 and Al_2O_3 films were deposited under varying process conditions and characterized using deposition rate, wet etch rate, and electrical measurements. Deposition rate was used to evaluate film growth behavior, while wet etch rate provided a relative indication of film density. Metal-oxide-semiconductor capacitors (MOSCAPs) were fabricated to evaluate electrical behavior using capacitance-voltage (C–V) and current-voltage (I–V) measurements. Together, these measurements establish preliminary relationships between ALD process conditions and resulting dielectric film properties and provide a foundation for continued optimization of the Oxford ASP.

Summary of Research:

This research investigated the quality of dielectric films deposited by atomic layer deposition (ALD), with emphasis on establishing baseline processes for the Oxford ASP and comparing its performance with the established Oxford FlexAL system. The study focused primarily on silicon dioxide (SiO_2) and aluminum oxide (Al_2O_3) films. Process variables included deposition temperature, oxide chemistry, deposition method, and ALD tool. Film quality was evaluated through deposition behavior, wet chemical etch behavior, and electrical characterization of fabricated metal-oxide-semiconductor capacitors (MOSCAPs).

ALD Film Deposition and Characterization

Overall, the deposition-rate measurements demonstrate measurable differences between the two ALD systems as well as temperature-dependent growth behavior.

Wet Etch Characterization

Wet chemical etching was used as an indirect method of comparing film density and chemical resistance. This data is drawn from the Oxford FlexAl.

For FlexAL Al_2O_3, the measured etch rate decreased with increasing deposition temperature as expected.

The FlexAL SiO_2 results displayed a different trend. The measured etch rate reached a maximum at the intermediate 200 °C deposition condition. Because this trend differed from the expected decrease in etch rate with increasing deposition temperature, additional measurements are required to determine its reproducibility.

MOSCAP Fabrication

MOSCAP devices were fabricated to characterize the electrical properties of the deposited dielectric films. The fabrication sequence consisted of wafer cleaning, ALD dielectric deposition, dielectric thickness measurement, patterned top-metal deposition, backside cleaning, backside-metal deposition, and electrical characterization. SiO_2 and Al2O3 dielectric layers were deposited using either the Oxford FlexAL. SiO2 films were deposited for device fabrication from the ASP while Al2O3 films were not available for deposition on the ASP. Top-metal electrodes were deposited through a shadow mask using the AJA Sputter, producing an array of circular MOSCAP structures with different electrode areas. Completed devices were electrically characterized using the Keithley Probe Station.

Electrical Characterization

Capacitance vs. voltage (C–V) measurements were performed to characterize the electrical response of the fabricated MOSCAP structures during a voltage sweep. The measured curves demonstrate transitions between accumulation, depletion, and inversion behavior. Both p-type and n-type silicon substrates were used during device fabrication, causing the direction and voltage of the C–V transition depending on substrate type. FlexAl film devices were constructed on p-type wafers while ASP devices were constructed on n-type wafers. This difference should be considered when comparing samples.

For the FlexAL Al_2O_3 samples, the 200 °C wafer exhibited a C-V transition voltage of approximately +0.88 V with a median hysteresis of 2.29 V, while the 300 °C wafer exhibited a median transition voltage of approximately +0.58 V and a lower median hysteresis of 1.01 V. This reduction in hysteresis suggests improved electrical stability at the higher deposition temperature.

The FlexAL SiO_2 sample deposited at 300 °C exhibited a transition voltage of approximately −3.05 V and a median hysteresis of 0.18 V. For ASP SiO_2, the 200 °C sample exhibited a transition voltage of approximately -4.79 V and median hysteresis of 1.07 V, while the 300 °C sample exhibited a transition voltage of approximately -4.05 V and median hysteresis of 0.62 V. The lower hysteresis measured at 300 °C suggests a possible improvement in electrical stability with increasing ASP deposition temperature.

Current vs. voltage (I-V) measurements were used to evaluate dielectric leakage.

The ASP results show a decrease in median leakage at the higher deposition temperature, although additional measurements are necessary for conclusivity.

Significant variation was observed in several I-V measurements when measuring the same size electrode, with leakage spanning multiple orders of magnitude. This variability may result from local dielectric defects, wafer nonuniformity, probe contact, electrode-area uncertainty, contamination, or fabrication effects such as shadow-mask bowing and unintended metal deposition beneath the mask. Based on acquired data, samples should be sorted to determine accuracy of each measurement. The electrical measurements should be considered preliminary indicators of process performance rather than definitive material properties. Additional device measurements and improved fabrication repeatability are recommended before establishing electrical baselines for the ASP.

Figure 1.

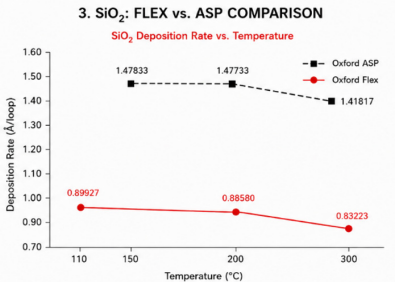

Figure 2.

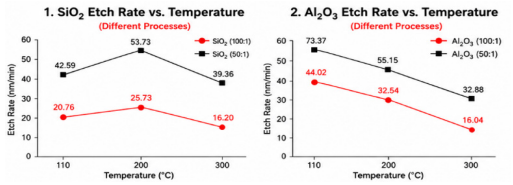

Figure 3.

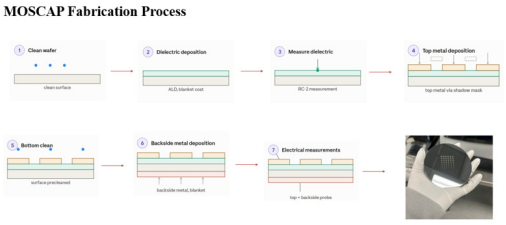

Figure 4.

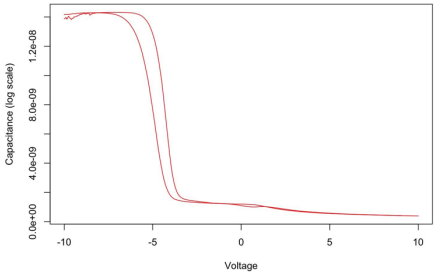

Conclusions and Future Steps:

This study established repeatable experimental procedures for ALD deposition characterization, wet etch testing, MOSCAP fabrication, and electrical measurement. The deposition results demonstrate that film growth rate depends on both deposition temperature and ALD system. Wet etch measurements further indicate that deposition conditions affect the chemical resistance of the resulting films, although the unexpected intermediate temperature behavior observed for FlexAL SiO_2 requires additional investigation. MOSCAP fabrication successfully enabled C-V and I-V characterization of selected dielectric films. These measurements provide an electrical complement to the deposition and etch-rate studies by evaluating the behavior of the dielectric within a functional device structure. MOSCAP construction and electrical measurements should be expanded to test a wider variety of oxide films. Upon further research, results will provide a complete comparison between the Oxford ASP and Oxford FlexAL and contribute to establishing baseline dielectric processes for the ASP system.

Tracking Light Atoms in 3D Ptychographic Reconstructions

CNF Summer Student: Helen Robinson
Student Affiliation: Department of Physics, University of Alabama at Birmingham

Summer Program(s): 2026 Cornell NanoScale Facility Research Experience for Undergraduates (CNF REU) Program

Principal Investigator(s): David Muller; School of Applied and Engineering Physics, Cornell University
Mentor(s): Steven Zeltmann

Primary Source(s) of Research Funding: NSF SUPREME REU

Contact: dm24@cornell.edu, hcrobins@uab.edu, steven.zeltmann@cornell.edu

Summer Program Website(s): https://www.cnf.cornell.edu/education/reu
Research Group Website: https://muller.research.engineering.cornell.edu/

Abstract:

As semiconductor devices move to 3D nanoscale architectures, traditional 2D imaging cannot fully characterize atomic-scale defects, interface roughness, and structural transitions in buried features. Multi-slice electron ptychography (MEP) addresses this by enabling 3D visualization with sub-Ångström lateral and nanometer-scale depth resolution. This project developed a program to test the depth resolution of Scanning Transmission Electron Microscopy (STEM) MEP reconstructions, using simulated and experimental datasets of gadolinium gallium garnet (Gd3Ga5O12, GGG) sectioned into depth-dependent slices. The program tracks and optimizes atomic coordinates across each slice and plots them in 3D to reconstruct the specimen's structure, calculating integrated pixel intensity within a mask at each atom to detect the ~1 nm z-axis spacing between oxygen atoms. This 3D positional information supports accurate predictive modeling and precise defect identification needed to advance next-generation semiconductor manufacturing.

Summary of Research:

STEM datasets are collected by rastering a focused electron beam across a sample and capturing the transmitted intensity, which traditionally yields only a 2D snapshot that neglects the sample's 3D structure. To recover depth information, the Muller Group uses MEP, a computational reconstruction technique requiring 4D STEM: the electron beam is defocused onto an Electron Microscope Pixel Array Detector (EMPAD), producing an overlapping diffraction pattern with two real-space (x, y) and two reciprocal-space (kx, ky) dimensions that encode the phase and amplitude needed to reconstruct the 3D structure. The Muller Group recently achieved 2.7 nm depth resolution, sufficient to visualize individual interstitial defects (Chen et al., 2024), and is now working toward one-nanometer and eventually sub-nanometer resolution to detect a broader range of defects, dopants, and interfaces. This project's objective was to determine whether STEM-MEP reconstruction can resolve the known 12.5 Å oxygen spacing in a garnet sample, and to develop a computational method to quantitatively compare simulated and experimental depth resolution.

GGG is a suitable test material because it contains isolated oxygen columns separated by 12.5 Å along the z-axis. Resolving individual oxygens within these columns would demonstrate depth resolution better than ~1 nm. To validate the code, I first reconstructed a simulated GGG dataset from the ideal crystal structure, sectioned into fifty 3.1 Å slices to match the experimental data. Each GGG unit cell has a central alternating Gd/Ga column surrounded by eight oxygen columns. A slight planar depth offset makes four columns appear brighter and four dimmer, a pattern that switches every two slices (6.2 Å). I tracked the central Gd/Ga column across all fifty slices using the AtoMap library's position-correction tools (Gaussian fitting and center of mass), then located the eight surrounding oxygen columns by branching outward at angles calculated from a Vesta GGG visualization. Because of this depth-dependent brightness pattern, I applied a mask to each tracked position and integrated the pixel intensity within it across the image slices, enabling detection of the true oxygen positions.

The resulting simulated reconstruction reproduced the expected four-bright/four-dim lateral pattern. Along each oxygen column, the 3D intensity projection showed a blinking pattern repeating every four slices (12.4 Å), just under the true 12.5 Å oxygen spacing, confirming depth resolution better than 12.4 Å. A line trace of intensity versus depth for a single oxygen column showed peaks spaced exactly four slices apart. Analyzing the heavier Gd/Ga corner columns, where Ga atoms are spaced 6.2 Å from Gd and 12.4 Å from the next Ga, showed the same four-slice peak spacing, meaning only the larger Ga–Ga spacing was resolved,

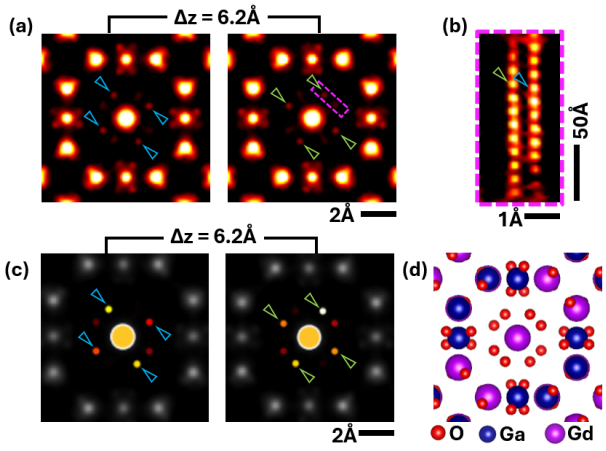

Figure 1: (a), (b), and (c) show simulated reconstructions of GGG based on the ideal crystal structure seen in (d). (a) and (c) are single 3.1 Å slices, two slices apart, from a fifty-slice stack. (a) shows the four-bright/four-dim pattern among the eight oxygen columns surrounding the central Gd/Ga column, caused by a z-axis depth offset between adjacent columns, shown in profile in (b).

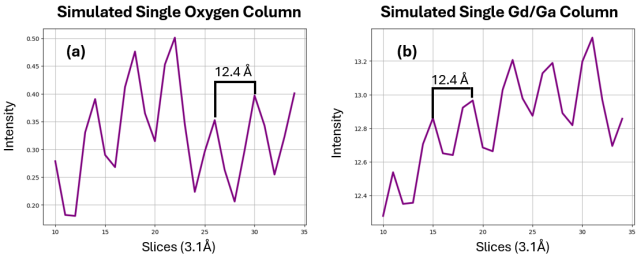

Figure 2: Integrated intensity vs. slice number for single atomic columns. (a) A single oxygen column, with peaks marking individual atoms spaced four slices (12.4 Å) apart, confirming accurate depth resolution. (b) A heavier Gd/Ga column, where only the larger Ga–Ga spacing (12.4 Å) is resolved; the smaller 6.2 Å Ga–Gd spacing is not detected.

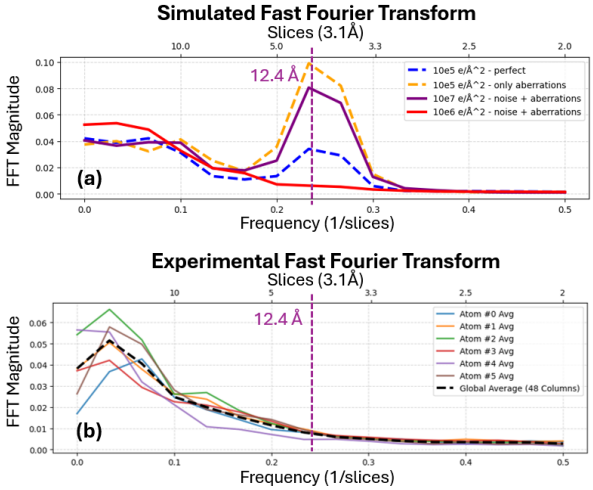

Figure 3: FFTs of oxygen column intensity traces, averaged across all eight columns per unit cell. (a) Simulated reconstruction, showing a clear 12.4 Å periodicity. (b) Experimental reconstruction, showing no corresponding periodicity.

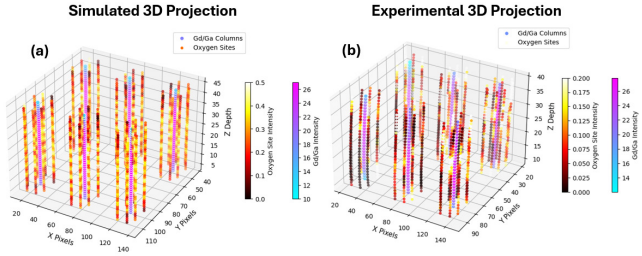

Figure 4: 3D reconstructions of atomic coordinates for the central Gd/Ga column and surrounding eight oxygen columns, from simulated (a) and experimental (b) data. Colormap indicates integrated pixel intensity within each atom's mask.

not the smaller 6.2 Å Ga–Gd spacing. This places the depth resolution between 6.2 Å and 12.4 Å. Taking the FFT of each oxygen column's line trace and averaging across all eight columns per unit cell produced a clear peak at four slices for the simulated dataset.

To identify which parameters most affect this depth resolution, I repeated this FFT analysis across multiple simulations of varying electron dose, noise, and aberrations, then overlaid the results. Most conditions still showed a 12.4 Å periodicity peak, but with varying amplitude, providing a guide to which parameters improve depth resolution.

Applying the same FFT analysis to the experimental scan showed no corresponding periodicity, indicating that the experimental reconstruction did not achieve the 12.4 Å depth resolution needed to resolve individual oxygen atoms.

Conclusions and Future Steps:

The program successfully tested depth resolution by first establishing expectations with a simulated dataset before comparing them to experimental results. This comparison showed that the experimental reconstruction did not reach the 1.24 nm depth resolution needed to resolve the oxygen sublattice in GGG. The simulation condition comparison provided valuable direction as the Muller Group continues refining STEM scan and MEP reconstruction parameters, using this program to evaluate future experimental datasets.

References:

[1] Karapetyan, S., et al. 3D atomic-scale metrology of strain relaxation and roughness in Gate-All-Around transistors via electron ptychography. Nat Commun 17, 3561 (2026).

[2] Chen, Z. et al. Imaging interstitial atoms with multislice electron ptychography. arXiv:2407.18063 (2024).

Niobium Seeded Tantalum Film Stress Characterization on AJA-Q

CNF Intern: Gavin Simoneau
Student Affiliation: Department of Mechanical and Mechatronics Engineering Technology, Rochester Institute of Technology (RIT)

Summer Program(s): 2026 Cornell NanoScale Facility Summer Internship
Mentor(s): Shilling Du, CNF
Primary Source(s) of Research Funding: NORDTECH
Contact: gavinsimoneau24@gmail.com, xd255@cornell.edu
Summer Program Website(s): https://www.cnf.cornell.edu/education/reu
Primary CNF Tools Used: AJA-Q2, FleXus Film Stress Measurement, Filmetrics R50, and the P7 Profilometer

Abstract:

This research investigated how niobium (Nb) and tantalum (Ta) sputtering pressures affect the stress and electrical properties of Nb-seeded Ta thin films intended for superconducting devices. The tested film structure consisted of approximately 5 nm of Nb beneath 100 nm of Ta on a silicon substrate. Nb deposition pressures of 3, 7, 15, and 20 mTorr were combined with Ta pressures of 3, 7, and 20 mTorr, creating 12 deposition conditions. Before deposition, each wafer received a MOS clean within four hours of being loaded into the deposition system. Film stress, thickness, deposition rate, and resistivity were evaluated for each condition. The results showed that both Nb and Ta deposition pressures influenced film stress. The 7 mTorr Nb and 7 mTorr Ta combination produced the lowest stress magnitude among the tested Nb-seeded film.

Summary of Research:

Tantalum is a promising material for superconducting devices because of its electrical and superconducting properties. However, its performance depends strongly on its crystalline phase. Alpha-phase tantalum is preferred because it has a resistivity of approximately 15–20 μΩ·cm and a superconducting transition temperature near 4.3 K. Beta-phase tantalum has a much higher resistivity of approximately 150–200 μΩ·cm and a transition temperature below 1 K. A thin Nb seed layer can promote the formation of the preferred alpha-Ta phase.

In addition to having low resistivity, a deposited film must have acceptable stress properties. Excessive tensile or compressive stress can contribute to wafer bow, film cracking, delamination, and variations during later fabrication processes. These problems can reduce device uniformity and process repeatability. The objective of this research was therefore to determine how Nb and Ta sputtering pressures affected film stress and to identify conditions that produced a low-stress film while maintaining desirable electrical properties.

Wafer preparation was an important part of the experimental procedure. Before deposition, each silicon wafer underwent a MOS clean. The clean was performed within four hours of deposition to limit the accumulation of airborne particles, organic residue, and other surface contaminants. Maintaining a clean wafer surface supported consistent film adhesion and uniform growth of the Nb seed layer and Ta film. Applying the same cleaning requirement to each wafer also helped reduce sample-preparation differences between deposition conditions.

The film stack consisted of approximately 5 nm of Nb followed by 100 nm of Ta. Four argon pressures were tested during Nb deposition: 3, 7, 15, and 20 mTorr. Each Nb pressure was paired with Ta pressures of 3, 7, and 20 mTorr. This created a matrix of 12 Nb–Ta pressure combinations. Ta-only films deposited at 3, 7, and 20 mTorr were also evaluated as baseline samples.

Film stress was determined by measuring wafer curvature before and after deposition using the FleXus stress-measurement system. The change in curvature was used to calculate the stress produced by the deposited film. Stress values closer to zero represented films with lower overall stress magnitude. Film thickness was measured to confirm the deposited thickness and calculate deposition rates. Electrical measurements were used to calculate resistivity and determine whether the films had properties consistent with alpha-Ta. Heat maps were then created to compare stress and resistivity across the tested pressure combinations.

The results demonstrated that deposition pressure had a substantial effect on film stress. For the Ta-only baseline samples, the 3 mTorr Ta condition produced the greatest stress magnitude. Increasing the Ta pressure

generally reduced the magnitude of the measured stress. A similar overall relationship was observed for the Nb-seeded films, although the Nb deposition pressure also influenced the final stress.

Among the Nb-seeded samples, the combination of Nb deposited at 7 mTorr and Ta deposited at 7 mTorr produced a stress value closest to zero. It was therefore identified as the lowest-stress Nb-seeded condition tested. Several films deposited at a Ta pressure of 20 mTorr also demonstrated relatively low stress. However, changing the Ta pressure did not produce the same response for every Nb pressure. This indicates that the conditions used to deposit the seed layer affected how the Ta film grew and how stress developed within the completed stack.

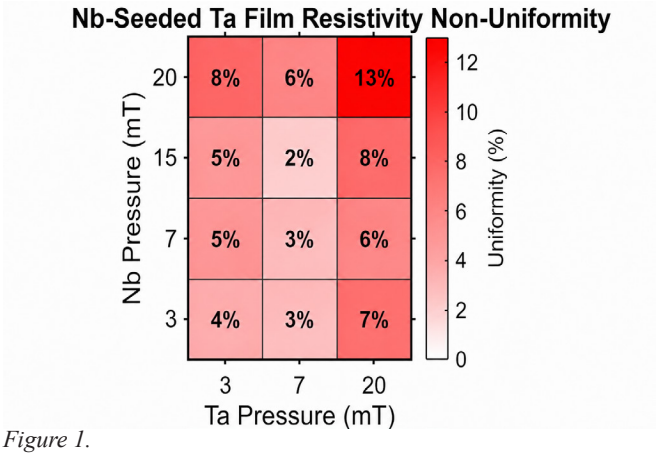

Figure 1.

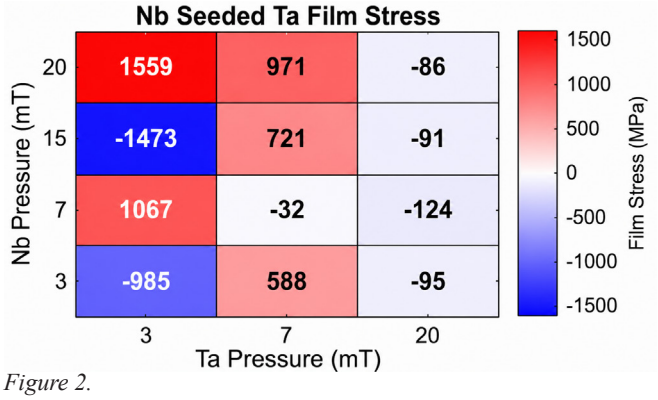

Figure 2.

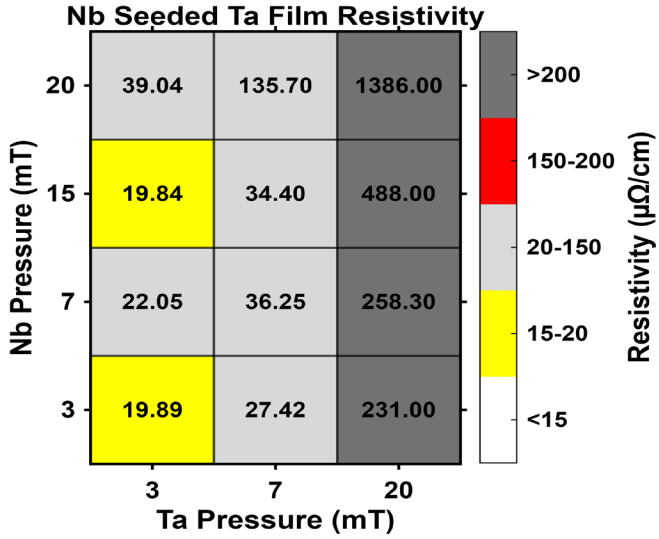

Figure 3.

The pressure matrix narrowed the range of promising deposition conditions and identified the region near 7 mTorr Nb and 7 mTorr Ta as a candidate for further study.

Stress could not be used as the only factor when selecting an optimized process. A film with low stress would still be unsuitable for superconducting-device fabrication if it had the high resistivity associated with beta-Ta. The preferred process must balance low stress, low resistivity, wafer-scale uniformity, and repeatability.

Conclusions and Future Steps:

This research showed that both Nb and Ta sputtering pressures influenced the stress of Nb-seeded Ta thin films. Increasing the Ta pressure generally reduced the magnitude of film stress, but the Nb seed-layer pressure also affected the completed film. Of the 12 combinations evaluated, the 7 mTorr Nb and 7 mTorr Ta condition produced the lowest measured stress magnitude.

Consistent wafer preparation was also necessary for comparing the samples. Performing a MOS clean within four hours of deposition helped maintain a clean surface and supported uniform film adhesion and growth. This cleaning requirement should be maintained in future experiments so that differences between samples are primarily caused by deposition conditions rather than surface contamination.

Future work should repeat the most promising conditions to determine whether the results are reproducible. Additional pressures near 7 mTorr Nb and 7 mTorr Ta should be tested to define the optimum process more precisely. Stress, thickness, and resistivity uniformity should also be measured across the wafer. Structural characterization can be used to confirm alpha-Ta formation, while low-temperature measurements can determine the superconducting transition temperature. Finally, superconducting test devices should be fabricated using the optimized film to determine whether lower stress improves device uniformity, performance, and reliability.

Investigations on Optical Microscopy Capabilities during Initiated Chemical Vapor Deposition(iCVD) Experimentation

CNF Summer Student: G. Karsten Strobel
Student Affiliation: Rose-Hulman Institute of Technology, Department of Physics, Optical Engineering, & NanoEngineering

Summer Program(s): 2026 Cornell NanoScale Facility Research Experience for Undergraduates (CNF REU) Program

Principal Investigator(s): Dr. Nicholas Abbott and Dr. Rong Yang; R.F. Smith School of Chemical Engineering, Cornell University

Mentor(s): Soumyamouli Pal, Shiqi Li

Primary Source(s) of Research Funding: NSF Future Manufacturing Research Grant (FMRG) Grant No. NNCI-2025233

Contact: nla34@cornell.edu , ryang@cornell.edu, sp2476@cornell.edu, sl2869@cornell.edu, strobegk@rose-hulman.edu

Summer Program Website(s): https://www.cnf.cornell.edu/education/reu

Research Group Website: https://nlabbottcornell.weebly.com/, https://theyanglab.com

Abstract:

In situ monitoring of reactive systems is essential for efficient research, allowing the observations made during trials to influence how the research will adjust and improve over time. It also limits the need to transport samples between devices, reducing the odds of outside contaminants/impacts disturbing the sample's features including size distribution and structure. However, real time imaging using optical microscopy in high vacuum systems is challenging owing to poor resolution of microstructures, significantly reducing the ability to characterize samples throughout the duration of synthesis. Here, we evaluate the constraints that lead to degradation of image quality during in situ optical imaging of an initialized chemical vapor deposition reactor system and establish image processing–based methodologies for improving the resolution of the synthesized microstructures. By capturing images across various physical arrangements of the system setup, we systematically isolate variables contributing to image degradation including external vibrations caused by the chamber's vacuum pump and the quartz glass cover used contain the reaction. The resulting images are processed and evaluated using ImageJ/Fiji to perform automated particle analysis and extract line-intensity profiles. These processed images are then quantitatively compared against high-quality reference images (ex-situ ground truth images) to assess the accuracy of the modified system arrangements and image processing techniques. Alongside this approach, a standard line-grating was imaged and compared under various reactor conditions to directly review the optical capabilities of the iCVD reactor. This test determined significant loss in optical resolution ability was attributed to distortion caused by the glass lid.

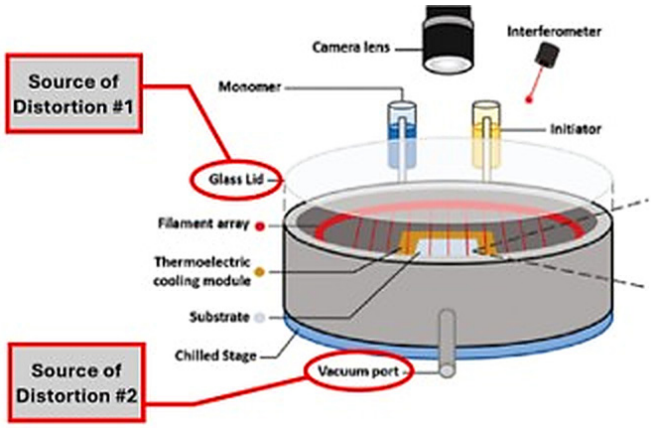

Figure 1: Labeled diagram of the iCVD reactor system studied. Two major sources of optical distortion are labeled.

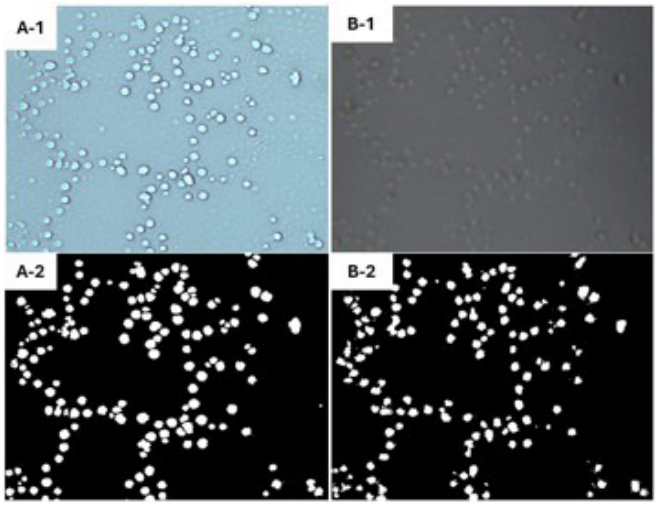

Figure 2: Initial attempts at segmentation and comparison between ex-situ(A) and in-situ(B) images.

Summary of Research:

The direct *ex-situ* to in-situ image comparison method proved certain limitations to certain methods involving computer-aided segmentation was not conclusive. Though the method was theoretically sound, comparing a software's ability to properly perform segmentation on a low-resolution in-situ image and compared to the corresponding high-resolution *in-situ* reference, several issues arose throughout attempts to pursue this task. The research was unable to feasibly utilize Fiji's trainable segmentation software to create a model with both flexibility and accuracy. When the models could identify and divide particles from images, they were unable to perform the same task for different image types (*in-situ vs ex-situ*), and vice versa.

The line-profile test proved much more conclusive. By imaging the standard line grating at maximum (500x)

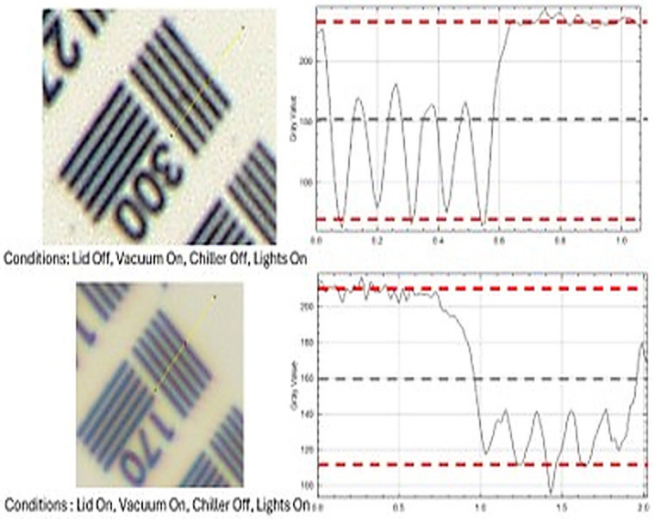

Figure 3: Visual aid displaying line-profile intensity analysis procedure with analysis images on left-hand side and corresponding gray-value plot on right-hand side.

magnification under specific conditions of the reactor (presence of glass lid, status of vacuum pump, status of chiller, & ambient lighting conditions), the measure of gray value was able to be extracted across the grating to determine what spacing of features was resolvable as seen in figure 3. By analyzing the line profiles and measuring to see a 50% gray value recovery relative to the average minimums(troughs) & maximum values, a consistent measure to claim whether the features were resolved was used to determine the relative contributions to distortion. The results expressed that both ambient lighting and external vibrations sourced from instruments besides the vacuum pump were both negligible, while the glass lid contributed significantly higher than all other sources of distortion. The presence of the glass lid reduced the microscope's capability to resolve images by nearly half (from being able to resolve features at 330 lines/mm down to only around 160 lines/mm). The main phenomena caused by these distortions were deduced to be chromatic aberration and some astigmatism as seen in figure 4. The vacuum pump's vibrations only contributed to approximately a 10% to 15% loss in resolving ability.

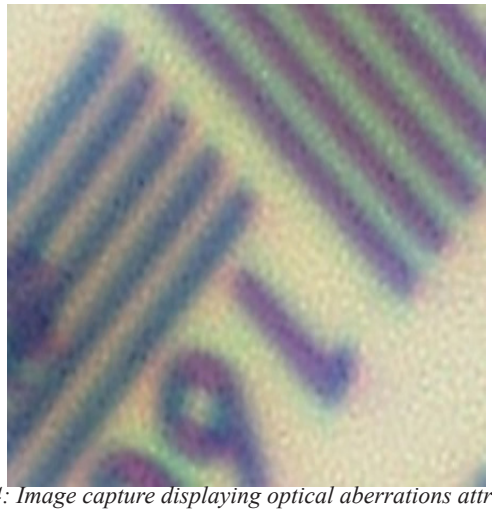

Figure 4: Image capture displaying optical aberrations attributed to glass lid.

Conclusions and Future Steps:

Future investigation should involve the application of any methods deemed appropriate to bypass/mitigate the optical distortion. Discussions within the group have began looking into cameras to be positioned within the chamber, bypassing the glass lid entirely, as well as potentially implementing monochromatic lighting to minimize chromatic aberration.

Acknowledgements:

I would like to thank the NSF Future Manufacturing Grant and Cornell University for the opportunity to participate in this research. I would also like to give thanks to Dr. Rong Yang & Dr. Nicholas Abbott for their guidance and lab space & equipment, as well as Dr. Soumyamouli Pal & Shiqi Li for their day-to-day assistance, training, and active support throughout the duration of this project.

References:

[1] Jain, A.; Pal, S.; Li, S.; Abbott, N. L.; Yang, R. Single-Step Synthesis of Shaped Polymeric Particles Using Initiated Chemical Vapor Deposition in Liquid Crystals. Sci. Adv. 2024, 10 (45), eadp5573 DOI:10.1126/sciadv.adp5573

[2] Park, Kwang-Won, Karen K. Gleason, and Rong Yang. Dec 30. 2024, "Advanced morphological control of polymeric surfaces using initiated chemical vapor deposition (iCVD)." Advanced Functional Materials 35, no. 24 (2025): 2417620.

[3] J. Schindelin et al., Fiji (Version 2.15.0). (2024). Accessed: Jul. 20, 2026. [Online]. Available: https://imagej.net/software/fiji/